

Synthesis, Structural, Morphological and Magnetic Properties of La and Mn Co- doped Bismuth Ferrite



Ambreen Afshan

Regn. # 173051

A thesis submitted in partial fulfillment of the requirements

for the degree of **Master of Science**

in

Physics

Supervised by: Dr. Syed Rizwan Hussain

Department of Physics

School of Natural Sciences



National University of Sciences and Technology

H-12, Islamabad, Pakistan

June, 2020

National University of Sciences & Technology**MS THESIS WORK**

We hereby recommend that the dissertation prepared under our supervision by: Ambreen Afshan, Regn No. 00000173051 Titled: Synthesis, Structural, Morphological and Magnetic Properties of La and Mn Co-doped Bismuth Ferrite Nanoparticles be accepted in partial fulfillment of the requirements for the award of **MS** degree.

Examination Committee Members1. Name: DR. FAHEEM AMINSignature:  _____2. Name: DR. MUDASSIR IQBALSignature:  _____External Examiner: DR. MUHAMMAD MUMTAZSignature:  _____Supervisor's Name DR. SYED RIZWAN HUSSAINSignature:  _____



 Head of Department

20/11/2021

 Date

COUNTERSIGNEDDate: 22-01-2021



 Dean/Principal

Dedication

This thesis is dedicated to my beloved father Mukhtar Ahmed and mother Zainab Mukhtar, without their encouragement and prayers this whole would have remained a dream

Acknowledgements

Foremost, I would like to thank Almighty **ALLAH**, the merciful and compassionate, for providing me strength and opportunity to complete this research.

My sincere gratitude goes to my supervisor **Dr. Syed Rizwan Hussain** for his continuous support, active guidance, motivation, patience and immense knowledge throughout my research. I am very thankful to principal of School of Natural Sciences **Dr. Rashid Farooq** and HOD Physics **Dr. Shahid Iqbal** for providing me this opportunity and for their assistance. Special thanks to my GEC members **Dr. Fahim Amin and Dr. Mudassir Iqbal** for their encouragement, guidance and insightful comments for the improvement of my work.

My special appreciation for my friends **Komal, Sabeen, Afsheen, Sabah, Sania, Sundas and Jameela** for their assistance and words of encouragement throughout my work. Thank you for their worthy support and cooperation and helping me survive all the stresses.

Last but not the least, Special thanks to my **entire family, my beloved parents**, my sister **Maryum**, my brothers **Shahbaz, Usman, Rizwan** and my husband **Muhammad Nadeem Shakoor** for standing with me through every thick and thin, for bearing with me and providing me emotional support during this research. It would not have been possible without their support and encouragement.

Ambreen Afshan

Abstract

Bismuth Ferrite (BiFeO_3) has gained significant importance recently due to its novel multiferroic properties. Owing to its unique physicochemical, optical and magnetic properties, it is extensively used in number of applications such as light-emitting diodes, ferroelectric solar cells, transformers and magnetic shielding. The present research focusses on a simple and easy approach for synthesizing mesoporous gyroidal nanostructures; a template-free technique employing double-solvent sol-gel method for fabrication of La and Mn co-doped BFO nanoparticles. Double solvents including ethylene glycol (EG) and acetic acid were employed in this technique. $\text{Bi}_{1-x}\text{La}_x\text{Fe}_{1-y}\text{Mn}_y\text{O}_3$ as BFO, $\text{Bi}_{0.90}\text{La}_{0.10}\text{FeO}_3$ (BLFO), $\text{Bi}_{0.90}\text{La}_{0.10}\text{Fe}_{0.95}\text{Mn}_{0.05}\text{O}_3$ (BLFMO-5), $\text{Bi}_{0.90}\text{La}_{0.10}\text{Fe}_{0.85}\text{Mn}_{0.15}\text{O}_3$ (BLFMO-15) and $\text{Bi}_{0.90}\text{La}_{0.10}\text{Fe}_{0.80}\text{Mn}_{0.20}\text{O}_3$ (BLFMO-20) were fabricated by optimizing the conditions in double-solvent sol-gel method. XRD technique was utilized to analyze the phase purity of formation. XRD results revealed that the phase of BFO changed from rhombohedral to orthorhombic by La and Mn co-doping. The structural and morphological analysis of nanoparticles by SEM illustrated the presence of well-ordered mesoporous gyroidal nanostructures in BLFO and BLFMO-5. However, with the increment in Mn concentration (BLFMO-15 and BLFMO-20), the network started degrading with loss of ordered porosity. Further, the presence of mesopores in all nanostructures was confirmed by BET analysis. Magnetic properties of pure BFO and co-doped BLFMO were explored by VSM that reported the increase in ferromagnetism upon La doping. The decrease in magnetization and enhanced coercivity with increased Mn concentration (BLFMO-20) suggests the presence of antiferromagnetic phase in these nanoparticles. The results overall suggest that different co-doped BFO mesoporous nanoparticles can be fabricated by employing simple, easy and economical approach for variable magnetic properties.

Contents

Chapter 1 Introduction	1
1.1. Nanoscience	1
1.2. History of nanoscience	1
1.3. Nanomaterials	2
1.3.1. Naturally occurring nanomaterials:	2
1.3.2. Engineered nanomaterials (ENMs):	2
1.4. Types of Engineered Nanomaterials	3
1.4.1. Carbon nanomaterials	3
1.4.2. Metal nanomaterials	3
1.4.3. Dendrimers	3
1.4.4. Composites	3
1.5. Dimensions of nanomaterials	3
1.5.1. Zero-dimensional nanomaterials (0-D)	4
1.5.2. One-dimensional nanomaterials (1-D)	4
1.5.3. Two-dimensional nanomaterials (2-D)	4
1.5.4. Three-dimensional nanomaterials (3-D)	4
1.6. Applications of nanoscience	5
1.6.1. Catalysis	5
1.6.2. Medical field	6
1.6.3. Health and personal care	7
1.6.4. Textiles and Fabrics	7
1.6.5. Energy	7
1.6.6. Electronics	8
1.6.7. Construction industry	8
1.6.8. Biology	8
1.7. Magnetic properties of nanomaterials	9
1.7.1. Diamagnetic materials	10
1.7.2. Paramagnetic materials	10
1.7.3. Antiferromagnetic materials	10
1.7.4. Ferromagnetic materials	10
1.7.5. Ferrimagnetic materials	11
1.8. Multiferroic materials	11

1.9. Bismuth Ferrite (BiFeO ₃)	12
1.9.1. Structure of BFO.....	13
Chapter 2 Literature Review	14
Chapter 3 Fabrication and Characterization of Nanoparticles.....	20
3.1. Synthesis process of nanoparticles.....	20
3.1.1. Top down Approach	20
3.1.2. Bottom up Approach	21
3.2. Characterization techniques for nanoparticles	23
3.2.1. Powder X-ray diffraction (XRD)	23
3.2.2. Vibrating Sample Magnetometer (VSM).....	27
3.2.3. Scanning Electron Microscopy (SEM).....	29
3.2.4. Brunauer-Emmett-Teller (BET) surface area analysis	32
3.3. Synthesis of La and Mn co-doped BFO nanoparticles (BLFMO)	34
3.3.1. Apparatus	34
3.3.2. Chemical Reagents.....	35
3.3.3. Procedure.....	35
Chapter 4 Results and Discussion	39
4.1. X-Ray Diffraction analysis	39
4.2. Vibrating Sample magnetometer (VSM).....	42
4.2.1. Saturation Magnetization (M _s):	43
4.2.2. Coercivity.....	46
4.3. Scanning Electron Microscopy (SEM).....	47
4.4. Brunauer-Emmett-Teller (BET) Surface area analysis.....	49
Conclusion	51
References	52

List of Abbreviations

2D	Two-dimensional material
ENMs	Engineered nanomaterials
XRD	X-Ray diffraction
SEM	Scanning electron microscopy
VSM	Vibrating Sample Magnetometer
BET	Brunauer-Emmett-Teller
BFO	Bismuth Ferrite
BLFO	Lanthanum doped Bismuth Iron Oxide
BLFMO	Lanthanum and Manganese doped Bismuth Iron Oxide
M_s	Saturation Magnetization
M_r	Remanent Magnetization
H_{EB}	Exchange bias
H_c	Coercivity
RT	Room Temperature
EC	Ethylene Glycol

List of Figures

Fig 1.1 Engineered nanomaterials (ENMs).....	2
Fig 1.2 Classification based on dimensions of nanomaterials (a) fullerene (b) nanowires (c) graphene (d) 3D structure.....	4
Fig 1.3. Nanoscience applications.....	5
Fig 1.4. Nano robot for medical science applications.....	6
Fig 1.5. Solar energy storage devices.....	7
Fig 1.6. World’s smallest computer.....	8
Fig 1.7. Orientations of magnetic moments in different materials.....	9
Fig 1.8. Multiferroic materials.....	12
Fig 1.9. Perovskite structure of BFO.....	13
Fig 3.1. Different approaches for synthesis.....	20
Fig 3.2. Scheme of sol-gel method.....	22
Fig 3.3. Bragg’s law.....	24
Fig 3.4. Working of XRD instrument.....	26
Fig 3.5. XRD instrument.....	27
Fig 3.6. VSM mechanism.....	28
Fig 3.7. Mechanism of sample-electron interaction.....	30
Fig 3.8. Working of SEM.....	31
Fig 3.9. SEM instrumentation.....	32
Fig 3.10. BET surface area analyzer.....	33
Fig 3.11. Flow chart for BLFMO Synthesis.....	36
Fig4.1. XRD for BFO, BLFO-(10%) and BLFMO-(5,15,20%) at room temperature.....	39
Fig4.2. Bragg peak shift in BLFMO.....	40
Fig4.3. M-H loops for BFO, BLFO (10%) and BLFMO-(5,15,20%) at room temperature.....	43
Fig4.4. Saturation magnetization vs pure and doped BFO.....	44

Fig4.5. Super-exchange effect between Fe^{+3} and Mn^{+2} 46

Fig 4.6. SEM images of (a) pure BFO sample (b) BLFO (c) BLFMO-5% (d) BLFMO-15%
(e) BLFMO-20%.....48

Fig 4.7. N_2 gas isotherms of (a) BFO sample (b) BLFO (c) BLFMO-5% (d) BLFMO-15%
(e) BLFMO-20% measured at 77K.....50

List of Tables

Table 3.1. Chemical Reagents used in synthesis of BLFMO.....	35
Table 4.1. Lattice strain calculated by Scherrer's formula.....	41
Table 4.2. Magnetic parameters of pure and doped BFO	45
Table 4.3. Surface area and pore size of various BFO nanostructures extracted from BET.....	50

Chapter 1

Introduction

1.1. Nanoscience

Nanoscience is manipulation and study of those materials that exhibit improved physicochemical properties owing to their nano scale size ranging from 10^{-6} m to 10^{-9} m. Nanocrystalline materials possess following distinct properties as compared to that of the bulk:

- Higher surface to volume ratio
- Size confinement
- Quantum effects
- Magnitude size reduction
- Coulomb blockade
- Predominance of interfacial

Nanoscience aims to study these novel properties of the nanomaterials [1].

1.2. History of nanoscience

The first discussion of the nanoscience dates back to the speech delivered by Richard Feynman in 1959 named as "There's Plenty of Room at the Bottom". He focused on the importance of "manipulating and controlling things on a small scale" and how they have ability to "tell us much of great interest about the strange phenomena that occur in complex situations". He explained how a physical phenomenon can be changed by changing the size. However, 'nanotechnology' was first used in 1974 paper by the Japanese scientists Norio Taniguchi, focusing on production technology to create objects at nanometer scale. Later, the K. Eric Drexler developed method molecular nanotechnology [2]

1.3. Nanomaterials

The Greek word “nano” means “dwarf” and it is a prefix for 10^{-9} . Nanomaterials are the chemical materials which are prepared at a very small scale and they must have at least one dimension less than 100 nanometers. These nanomaterials exhibit novel physical, electrical, chemical, optical, magnetic, and other properties as compared to the bulk [3]. Nanomaterials comes from two sources:

1.3.1. Naturally occurring nanomaterials:

These nanomaterials come from volcanic ash and as a by-product of combustion processes (e.g. welding, diesel engines). They are named as “ultrafine particles” and are very heterogenous substances based on their physicochemical properties.

1.3.2. Engineered nanomaterials (ENMs):

The materials that are intentionally engineered on the nanoscale to get desired physicochemical properties for a specific purpose are called engineered nanomaterials. This makes them promising for applications in number of fields [4]

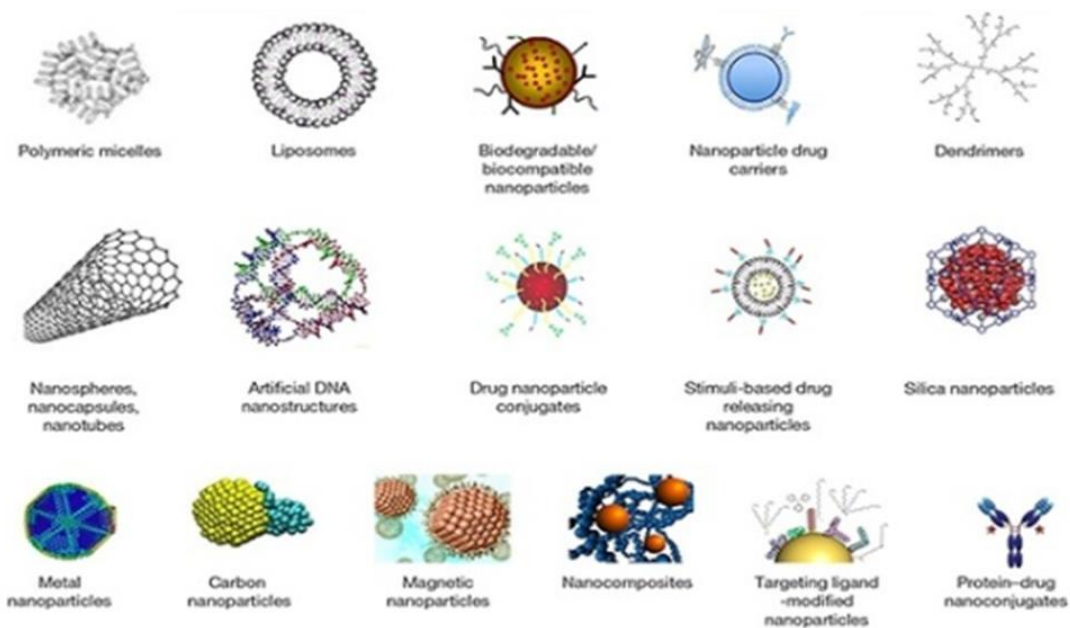


Fig 1.1 Engineered nanomaterials (ENMs) [5]

1.4. Types of Engineered Nanomaterials

There are many different types of engineered nanomaterials. However, the current four types are:

1.4.1. Carbon nanomaterials

These materials are mostly composed of carbon. They usually occur as tubes, ellipsoids and hollow spheres. Among these, the spherical ones are known as fullerenes, whereas nanomaterials that are cylindrical in shape are named as nanotubes. These carbon nanomaterials find extensive applications in electronics, films and coatings.

1.4.2. Metal nanomaterials

These materials consist of metal oxides, nanogold, quantum dots and nanosilver. A quantum dot is a semiconductor crystal made up of many atoms of nanometer size. Their optical properties can be changed by varying their size.

1.4.3. Dendrimers

Dendrimers are the nanosized nanomaterials and are prepared from the branched units. Their surface consists of several chains ends that can help to carry out important chemical functions. This unique behavior makes it very useful for functions like catalysis and drug delivery. The interior cavities present in the three-dimensional dendrimers can hold and take the drug to the required site, thus helping in drug delivery process.

1.4.4. Composites

Nanomaterials are joined to each other or with the larger bulk nanomaterials by composites. Various properties of auto parts like their mechanical, thermal and flame-retardant properties are improved by adding nanosized clays in them. [6]

1.5. Dimensions of nanomaterials

Nanomaterials are categorized into four types based on their elemental dimensions.

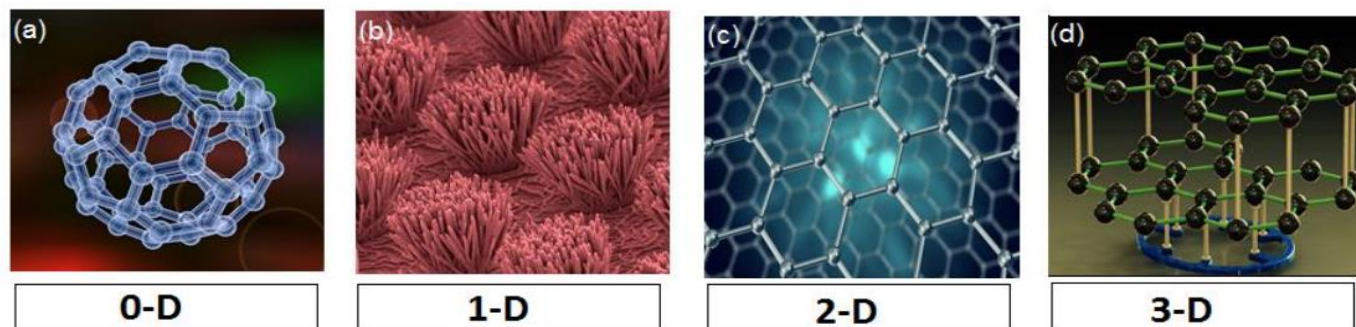


Fig 1.2 Classification based on dimensions of nanomaterials (a) fullerene (b) nanowires (c) graphene (d) 3D structure [7]

1.5.1. 0-D nanomaterials

The materials in which all the dimensions are present in the range of nanoscale (no dimension is greater than 100 nm) are classified as 0-D nanomaterials. In these nanomaterials, the electrons motion is restricted in all three directions. Zero-dimensional nanomaterials include sphere, nanoclusters and nano dispersions.

1.5.2. 1-D nanomaterials

The materials consisting of one of the dimensions outside the range of nanoscale are known as 1-D nanomaterials. This results in the formation of needle like nanomaterials. In such system, electrons can move in one direction but are restricted in other two directions. Common examples of 1-D nanomaterials are nanotubes, nanowires and nanorods.

1.5.3. 2-D nanomaterials

The nanomaterials consisting of two of the dimensions outside the range of nanoscale are 2-D nanomaterials. This results in the formation of plate-like shaped nanomaterials. In such system, electrons can move in two directions but show restriction in one direction. 2-D nanomaterials consist of nanofilms, nanolayers, and nano coatings.

1.5.4. 3-D nanomaterials

These materials also called bulk nanomaterials, have no dimension confined to nanoscale range. All the three dimensions in 3-D nanomaterials are greater than 100nm. The electrons have freedom to move in all three directions. Nanosized crystals combine in

multiple arrangements and different orientations to give rise to the bulk nanomaterials. In powders, multilayer, fibrous and poly crystalline materials, 0D, 1D and 2D elements tend to remain close and form interfaces [8,9]

1.6. Applications of nanoscience

Nanomaterials have multiple applications in our daily life due to their extraordinary and unique properties. Nanoscience is playing an important role in technological advancement and industrial revolution. Some of the applications of nanomaterials are discussed below:



Fig 1.3. Nanoscience applications [10]

1.6.1. Catalysis

- When combustion of diesel fuel takes place in engine, incomplete oxidation takes place and results in the formation of particles of carbon, unreacted fuel and carbon monoxide. In order to avoid this, the nanoparticles of Cerium (IV) oxide when added to diesel in small amount forms a homogenous mixture with the fuel. In this way, it acts as a

heterogenous catalyst to ensure that complete combustion takes place. Complete combustion forms only carbon dioxide and water. In this way, Cerium (IV) oxide nanoparticles improves the efficiency of engine and reduces pollution.

- Nanoparticles of alloys of palladium and rhodium are added as a catalyst in cars.

1.6.2. Medical field

The properties like extremely small size and ability to move makes nanoparticles potential for applications in medical science. This includes:

- In the field of biomedical imaging, nanomaterials are being used as an image enhancer.
- In nano surgery, biological microelectromechanical devices (bioMEMS) are used to deliver desired drugs to the required areas.
- Nanoparticles are used as an imaging probe. In this process, nanocarriers of size ranging from 2-10 nm are used to deliver the imaging agent to the desired site i.e. cancer cells. Thus, help in determining the exact location of the cancerous cells and aids in medical treatment.
- Gold nanoparticles are resistant to corrosion. These nanoparticles present at the site of cancerous cells are heated up using radiations and are used to destroy nearby cancerous cells.

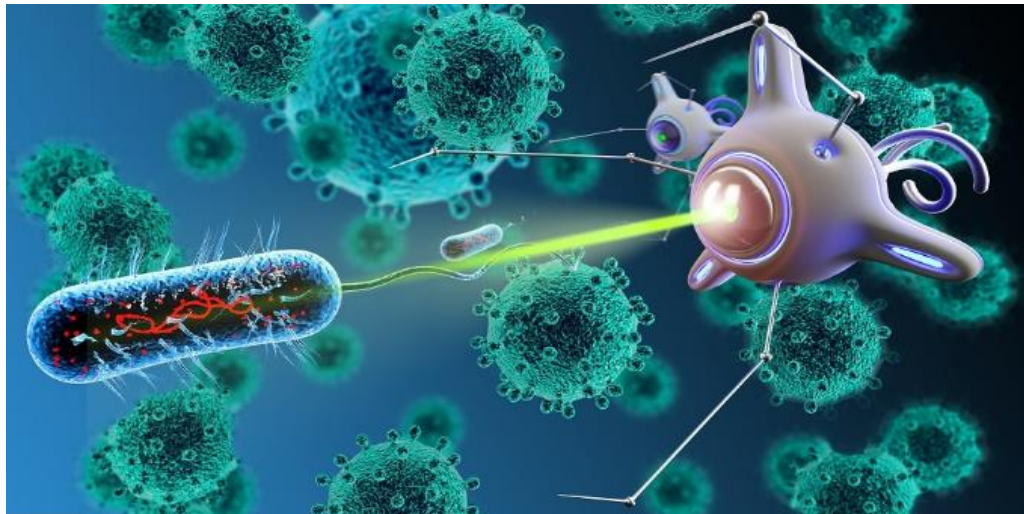


Fig 1.4. Nano robot for medical science applications

1.6.3. Health and personal care

- Nanoparticles because of their high surface areas are being used in cosmetics like sun-blocks/lotions and anti-aging creams.
- Silver nanoparticles are used in baby food cartons to avoid cross-contamination. They are also used in fabric dressings.
- Titanium dioxide nanoparticles contain Manganese (II) oxide in small quantities and are added in sun lotions which help to absorb UV radiations.
- Nanoparticles are used to deliver vitamins. In this way, help to soften the skin and thus reduces wrinkles.
- Silver and Zinc oxide nanoparticles have anti-microbial/anti-bacterial properties and are added to some skin care products.

1.6.4. Textiles and Fabrics

- The 'fleece' fabric is prepared by using carbon nanoparticles. These nanoparticles are embedded in the fabric instead of forming a coating.
- The properties of nanoparticles like highly absorbent, surface modifications of the nanoparticles and high surface areas give unique characteristics to fabrics including anti-bacterial, deodorizing, thermal-regulating, anti-fungal, and softness [11].

1.6.5. Energy

- Nanoparticles are used in solar energy storage devices
- New fuels i.e. carbon nanotube fuel cells are prepared using nanoparticles

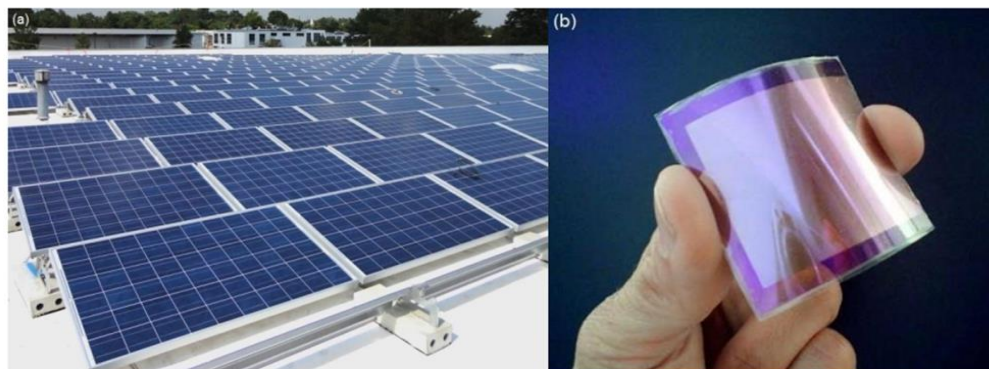


Fig 1.5. Solar energy storage devices

1.6.6. Electronics

- Nanomaterials are employed in formation of nanoelectronics device, solar cells, flat panel display and electrodes.
- Nano material magnets are used in the electrical circuits to reduce the power consumption.

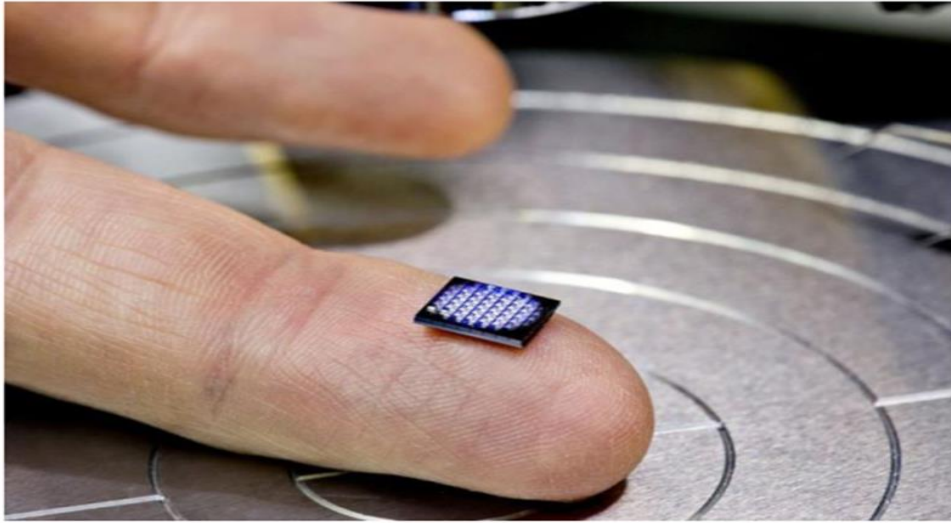


Fig 1.6. World's smallest computer

1.6.7. Construction industry

- Aerogel is composed of silica nanoparticles and is used as an insulating material for walls.
- Carbon nanotubes is used to fill the voids that occur in concrete. Thus, helps to eliminate cracks formation.

1.6.8. Biology

- Nanomaterials are used in biosensors and bio detectors.
- Nanoscale pores are used to separate molecules by size [12]

1.7. Magnetic properties of nanomaterials

Depending on the behavior of the materials for an applied magnetic field H , nanomaterials are classified as:

- Paramagnetic
- Diamagnetic
- Antiferromagnetic
- Ferrimagnetic
- Ferromagnetic

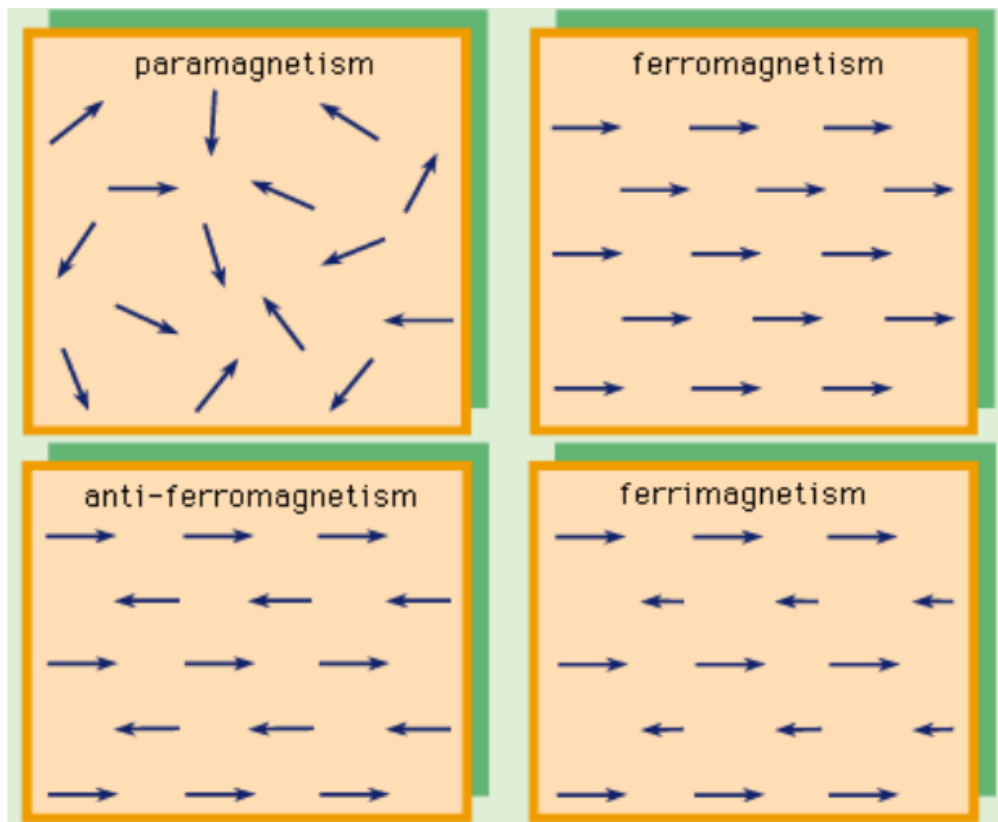


Fig 1.7. Orientations of magnetic moments in different materials

1.7.1. Diamagnetic materials

It is the phenomena in which when a material is subjected to an external magnetic field, the electrons of the atomic orbitals oppose the magnetic field and a dipole moment is induced in the direction which is opposite to the externally applied magnetic field. The induced moment is temporary and diminishes in the absence of magnetic field. Materials that possess closed electron subshells shows diamagnetism. These types of materials are weakly repelled on application of magnetic field. Copper, silicon, alumina, silver and gold are diamagnetic at room temperature.

1.7.2. Paramagnetic materials

The materials in which each atom possesses permanent magnetic moment due to incomplete/partial cancellation of electron spins are called paramagnetic materials. When the externally applied magnetic field is absent, they show random alignment of their individual magnetic moments and thus, possess no net magnetization as shown in Fig 1.7. However, on application of external field, these magnetic moments align themselves in the direction of magnetic field and thus possess nonzero magnetization. On removal of external magnetic field, the magnetization diminishes. Paramagnetic materials include aluminum, sodium, titanium and chromium.

1.7.3. Antiferromagnetic materials

The type of materials in which antiparallel alignment of magnetic spins result in no net magnetic moment are called antiferromagnetic materials. Such materials are diamagnetic in nature at absolute zero and become paramagnetic above a certain temperature called Neel's temperature.

1.7.4. Ferromagnetic materials

In these materials, the presence of parallel alignment of magnetic spins does not allow cancellation of electron spins are called ferromagnetic materials. This results in the permanent net magnet moment even in complete absence of external magnetic field. The permanent magnetic moment exists due to the mutual spin alignment over large volume

regions of the crystal called domains. Above Curie temperature, material loses ferromagnetism and exhibits paramagnetism.

1.7.5. Ferrimagnetic materials

Ferrimagnetism is a kind of antiferromagnetism in which antiparallel spins of different magnitudes are present in the material. Due to the different magnitudes of spins, the material possesses magnetic moment even when external field is not applied. These materials behave ferromagnetically below Neel's temperature and become paramagnetic above this temperature. [13]

1.8. Multiferroic materials

Multiferroics is new class of magnetoelectric materials, and in them the ferroelectricity, ferromagnetism and ferro elasticity coexists (Fig 1.8). Multiferroic materials are of great interest to study the mechanisms leading to this magnetic-ferroelectric coupling and for the application of these order parameter couplings in novel devices. Multiferroic materials have wide applications in information storage, sensors and spintronic devices because of their increased, faster and efficient ability of storing and retrieving data.

In multiferroic materials, the transition metals ions (i.e. iron/nickel) gives rise to the magnetic polarization whereas the ions shifting their position due to interaction with neighbor atoms produces the electric polarization [14]

Some of the examples of multiferroic materials include BiFeO_3 , BiMnO_3 and TbMnO_3 .

BiFeO_3 (BFO) belongs to the single-phase multiferroics and are extensively studied owing to its high Curie and Neel temperature i.e. $T_C = 820^\circ\text{C}$ and $T_N = 370^\circ\text{C}$ respectively.

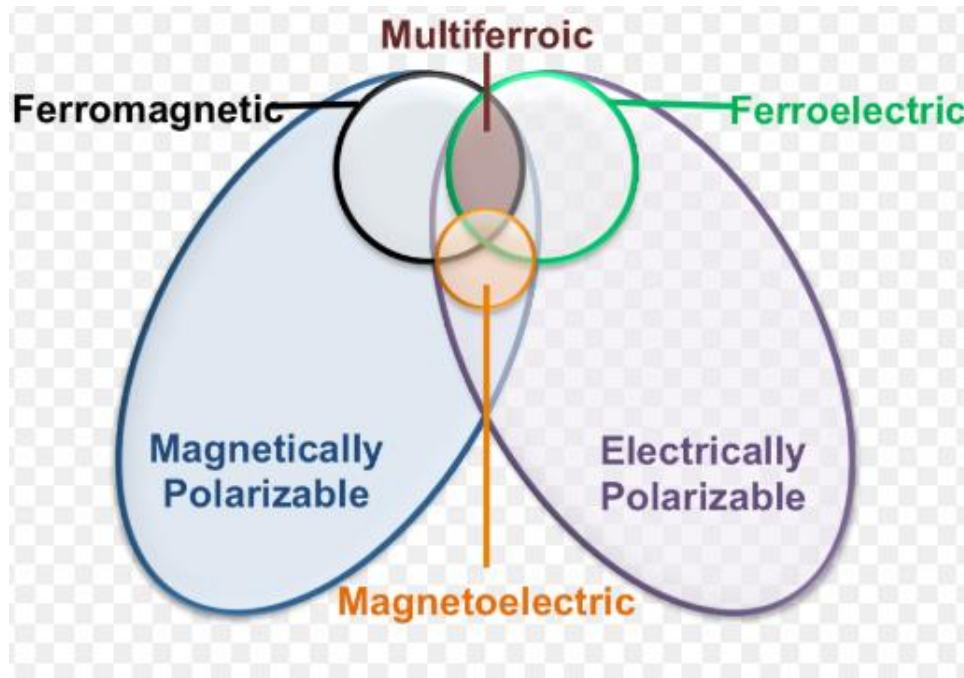


Fig 1.8. Multiferroic materials [15]

1.9. Bismuth Ferrite (BFO)

BFO being multiferroic material possess both ferroelectricity and magnetism at room temperature. Usually in multiferroic materials, ferroelectricity is caused by the vacant d^0 orbitals whereas ferromagnetism is produced due to the partially filled d^n orbital. In BFO, ferroelectricity occurs because of lone pair of electrons in $6s^2$ orbital of Bi^{3+} ion. Whereas, ferromagnetism is present due to Fe^{3+} ions. BFO is widely studied because it has high Curie and antiferromagnetic Neél temperature i.e. $T_C = 820^\circ\text{C}$ and $T_N = 370^\circ\text{C}$ respectively.

BiFeO_3 exhibits G-type antiferromagnetism and spin cycloidal structure. G-type spin structure arises due to the transition metal Fe^{3+} . Each Fe^{3+} ion having up spin is surrounded by six neighboring Fe^{3+} ions having down spin. As these spins do not show perfect antiparallel alignment, a weak canting moment is present which produces net magnetic moment. This canted spin exists in the form of a spin cycloid which repeats itself after a long distance of 62-64nm [13].

1.9.1. Structure of BFO

BFO exhibits perovskite structure which is rhombohedrally distorted in the [111] direction and an $R3c$ space group at RT. The lattice parameters of rhombohedral perovskite structure are $a = b = c = 5.63 \text{ \AA}$ and $\alpha = \beta = \gamma = 59.4^\circ$. Perovskite structures are demonstrated by a general formula ABO_3 , in which A and B represents cations and O is the anion. In BiFeO_3 , Bismuth atoms are present at the octahedral sites, iron atoms located at B sites are surrounded by oxygen atoms situated at all six faces and gives rise to FeO_6 Octahedral. The structure of BFO is shown below (Fig 1.9)

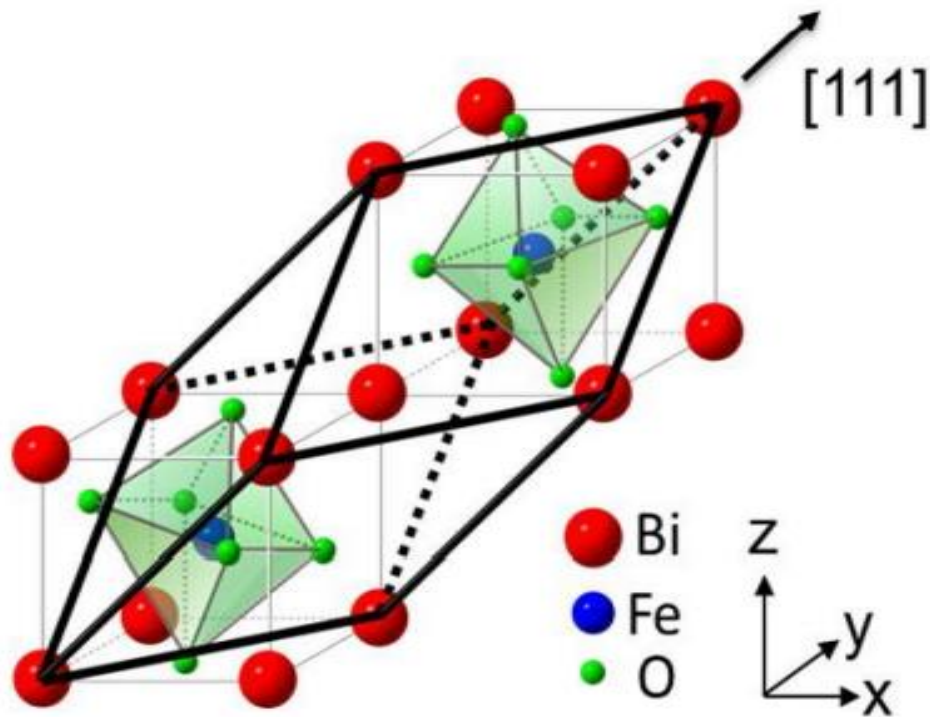


Fig 1.9. Perovskite structure of BFO [13]

Chapter 2

Literature Review

Syed Irfan et al. fabricated the template-free gyroid-like mesoporous nanostructures by co-doping Lanthanum and Manganese in BFO and studied their improved photocatalytic activity. For this purpose, $\text{Bi}_{1-x}\text{La}_x\text{Fe}_{1-y}\text{Mn}_y\text{O}_3$ at different concentrations of La and Mn ($x = 0.0, 0.10$; $y = 0.0, 0.05, 0.15, 0.20$) were prepared by double solvent sol-gel method. Ethylene glycol (EG) and acetic acid were employed as solvents in the process. X-ray diffraction pattern revealed the transition from rhombohedral to orthorhombic phase by increasing the concentration of Mn dopant. This may be related to the decrease in grain size caused by ionic radii mismatch of dopant and host. FESEM indicated the presence of well-ordered gyroid-like mesoporous nanostructure network in BLFMO-5 and BLFMO-15 sample. Moreover, the BLFMO-5 sample showed increased photocatalytic activity in comparison with pure BFO. Co-doped BFO nanoparticles showed higher degradation rate of dye as compared to the pure BFO. This paper presented an easy approach to synthesize mesoporous and well-ordered nanostructures for numerous applications [16].

Sunil Chauhan et al. in 2013 reported the structural, dielectric, optical and magnetic properties of Barium (Ba) doped BFO nanoparticles. $\text{Bi}_{1-x}\text{Ba}_x\text{FeO}_3$ nanoparticles at different concentrations of Ba ($x=0.05, 0.10$ and 0.15) were prepared using the sol-gel method. X-ray diffraction analysis indicated the presence of distorted rhombohedral phase in Ba-doped BFO (except in $x=0.05$ sample). This distortion was attributed to the increase in unit cell volume and particle size due to Ba doping. Raman and FTIR spectra also proved the distortion in the BFO structure caused by Ba. The doped nanoparticles showed ferromagnetism at room temperature and enhanced remanent magnetization. This may be ascribed to the presence of uncompensated spin moments and structural distortion. UV results revealed that Ba substitution can help in tuning of band gap in visible range. Further techniques reported the

presence of magnetoelectric coupling in Ba-doped BFO. This paper presented an important candidate possessing enhanced magnetic properties and tunable optical band gap for the use in many novel applications [17].

Z. X. Cheng et al. in 2007 investigated the structural, magnetic and ferroelectric properties of the La-doped Bismuth Ferrite (BFO). For this purpose, La-doped $\text{Bi}_{1-x}\text{La}_x\text{FeO}_3$ nanoparticles by varying concentrations of La as $x=0, 0.1, 0.2,$ and 0.3 were prepared via solid state reaction. X-ray diffraction patterns of $\text{Bi}_{1-x}\text{La}_x\text{FeO}_3$ revealed that undoped and $x=0.1$ doped BFO exhibited rhombohedrally distorted perovskite structure whereas at $x=0.2,$ it underwent phase transition to $C222$ orthorhombic symmetry and at $x=0.3,$ it transformed to $P4mm$ tetragonal symmetry. Moreover, a significant reduction in electric leakage was observed by La-doping. La-doped BFO showed enhanced ferromagnetism that can be attributed to the disruption of spin cycloid structure caused by structural changes. In conclusion, La-doped BFO exhibited enhanced ferroelectric and magnetic properties and can be used in number of applications [18].

Jia-Huan Xu et al. in 2008 studied the synthesis of BFO using sol-gel method at a low temperature of 450°C . The ethylene glycol was employed to control the ionic concentration of mixture. The identification of compounds and the decomposition process was studied using GC/MS, DSC-TG and infrared spectrometry techniques. X-ray diffraction was carried out to study structural morphology. XRD provided the information about phase transformation of BFO, which started at the temperature as low as 400°C and the complete crystallization of BFO into the perovskite structure took place at temperature of 450°C . Further, scanning transmission electron microscopy (STEM) and high-resolution TEM was used to identify the crystalline features of BFO. STEM results showed that crystallites having size less than 10nm were present in the form of tiny dark spots in the amorphous matrix [19]

Shan-Tao Zhang et al. in 2006 reported the phase transition and enhanced multiferroic properties due to lanthanum doping in BFO ceramic. $\text{Bi}_{1-x}\text{La}_x\text{FeO}_3$ at different

concentrations of Lanthanum ($x=0.05, 0.10, 0.15, 0.20, 0.30,$ and 0.400) were synthesized. It was observed that phase transition of BFO from rhombohedral to orthorhombic took place at lanthanum concentration $x=0.30$. It was further observed that this phase transition resulted in disruption of spin cycloid structure, releasing the locked magnetization and thus improving the multiferroic properties of BLFO [20]

Tae-Jin Park et al. in 2006 observed size dependent magnetic properties of BiFeO_3 . In their research, BiFeO_3 nanoparticles were prepared using facile sol-gel methodology and the magnetic properties were analyzed using the SQUID magnetometer. The important conclusions drawn from the study were that the enhanced suppression of spin cycloid structure of BFO is associated with the decrease in the size of nanoparticles. The size-restriction of nanoparticles at room temperature can result in increased magnetization values. Moreover, the leakage problem in BFO is caused by the oxygen vacancies. Thus, multiferroic behavior and resistivity can be enhanced by suppressing the oxygen vacancies in BFO system [21]

A. Mukherjee et al. in 2013 investigated the enhanced magnetic, electric and magneto-dielectric (MD) properties of BiFeO_3 upon gadolinium doping. Bismuth ferrite nanoparticles were prepared by sol-gel method. X ray diffraction and transmission electron microscopy (TEM) techniques were performed to study the phase purity of samples. The enhanced dc electrical resistivity was associated with variable range hopping conduction mechanism. Whereas, the variation of ac conductivity was attributed to the correlated barrier hopping (CBH) conduction mechanism. It was concluded that disruption of spin cycloid structure caused by the smaller crystallite size and the suppression of oxygen vacancies lead to these enhanced multiferroic properties [22]

Zhiwu Chen in 2011 discussed the low temperature synthesis of lanthanum doped BFO. $\text{Bi}_{1-x}\text{La}_x\text{FeO}_3$ doped nanoparticles were prepared at different concentrations of lanthanum as $x = 0, 0.15, 0.3, 0.4$ via sol-gel-hydrothermal route. The structural

characterization was performed using XRD, SEM, and FT-IR. The XRD results indicated that the BFO crystallites were obtained at the lanthanum concentration of $x \leq 0.3$ whereas the phase purity was dependent on the mineralizer concentration. SEM results indicated that morphology of the BFO nanoparticles can be controlled by varying KOH concentrations [23]

S.J. Lee et al. in 1999 synthesized barium titanate (BaTiO_3) and barium orthotitanate (Ba_2TiO_4) through polymerization complexation reaction using ethylene glycol (EG). The calcination at 700°C for 1 h resulted in the crystallization of BaTiO_3 powder (size of 100nm) from amorphous to tetragonal phase. Crystallization of Ba_2TiO_4 powder from amorphous phase required more time or higher temperature as compared to the BaTiO_3 . Dilatometry and differential scanning calorimetry revealed that phase transformation between monoclinic symmetry at low-temperature to orthorhombic symmetry at high-temperature takes place in the case of Ba_2TiO_4 . This phase transformation is accompanied by 5% volume decrease. 6 wt% magnesia (MgO) stabilizer can be used to maintain the high temperature orthorhombic at room temperature [24]

Sunil Chauhan et al. in 2011 prepared the Mn doped- BiFeO_3 (5, 10 and 15 mol%) by sol-gel method and studied the multiferroic, magnetoelectric and optical properties of doped nanoparticles. Structural characterization by XRD indicated that doped nanoparticles showed phase transition from rhombohedral to orthorhombic at the 15 mol% of Mn. The size of particles of doped BFO were measured in range of 50–200 nm. Ferromagnetic property was found to be increasing with an increase in Mn dopant concentration. The enhanced remanent magnetization ($2M_r$) value from 0.08 emu/g to 0.51 emu/g with the increased Mn concentration (5 to 15 mol%) was attributed to the disruption of spin cycloid structure caused by Mn doping. Magnetocapacitance value was also found to be increasing from 1.46% to 2.6% as the concentration of Mn in nanoparticles was increased from 5 to 15 mol%, indicating that Mn doping causes an improvement in multiferroic properties of BFO nanoparticles. Also, the optical properties of doped nanoparticles were studied by analyzing the photoluminescent properties [25]

Surbhi Gupta et al. in 2012 fabricated the Mn doped nanoparticles by chemical solution deposition process. The BFO nanoparticles were prepared by increasing the Bi concentration from 0 to 15% and Mn dopant from 0 to 20% and the effect of these two factors on the structural, ferroelectric, and magnetic properties of BiFeO₃ (BFO) was studied. It was found that 5% excess Bi resulted in no detectable change, whereas the 10% excess Bi caused the phase transition from rhombohedral phase. Piezo response force microscopy technique was performed to study the ferroelectric properties and indicated that the samples containing 5% excess Bi and 10% Mn dopant exhibited good ferroelectric properties. VSM results revealed that 10% Mn doped BFO possessed ferromagnetic behavior. It was concluded that 10% Mn doped BFO exhibit good multiferroic properties and are a potential candidate for applications in magnetic memories [26]

G S Arya et al. in 2012 employed combustion route using ethylene glycol to synthesize Bi_{1-x}In_xFe_{1-y}Mn_yO₃ co-doped nanoparticles. XRD results revealed that the rhombohedral structure existed in both undoped BFO samples and co-doped nanoparticles. However, some structural distortion is found to be caused by Indium and Manganese doping. The reduction in grain size and improvements in surface morphology caused by the In and Mn doping leads to the enhanced magnetic and electrical properties of these nanoparticle. The saturation magnetization in the case of pure BFO was found to be 0.20 emu/g and increased to 3.50 emu/g upon co-doping. It is concluded that this improved saturation magnetization occurs due to the reduction in grain size caused by doping. The co-doping decreases the magnetocrystalline anisotropy and thus magnetic coercivity decreases to 32 Oe. The dielectric properties were found to be changed by In and Mn co doping owing to the improvements in dielectric loss. All the doped samples possessed high resistivity of the order of 10⁹ Ω cm, that can be related to the reduction in grain size and oxygen ion vacancies [27]

F. Gonzalez Garcia et al. in 2009 synthesized lanthanum doped Bismuth Ferrite BiFeO_3 via soft chemistry route and observed the lanthanum concentration effects on the grain size, morphologies and phase formation of doped BFO nanoparticles. X ray diffraction pattern revealed the presence of perovskite structure at 850°C temperature. Infrared results showed presence of no carbonates. Raman analysis indicated that lanthanum substituted bismuth atoms in BFO. Scanning electron microscopy was performed to get an idea about morphology of nanoparticles. SEM images indicated the formation of homogenous sized nanoparticles [28].

Chapter 3

Fabrication and Characterization of Nanoparticles

3.1. Synthesis process of nanoparticles

There are several methods to synthesize and fabricate nanoparticles. Two main approaches for the fabrication of nanoparticles (shown in Fig3.1) are as follows:

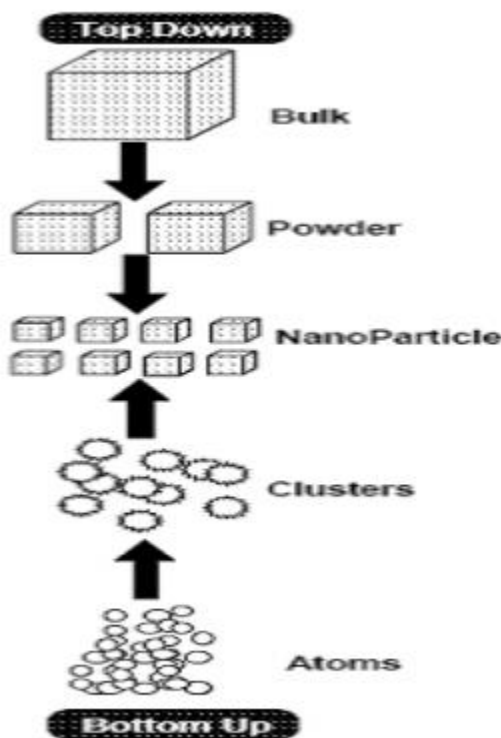


Fig 3.1. Different approaches for synthesis [29]

3.1.1. Top down Approach

Top down approach starts with the bulk or the large piece and then smaller components are produced using some mechanical, chemical or other forms of energy [29]. The desired structure is obtained by breaking and reforming atoms of complex structure. Some of the methods implemented for fabrication of nanoparticles in top down approach are:

- Electrospinning

- Ball milling
- Laser ablation
- Chemical etching
- Electro-explosion

3.1.2. Bottom up Approach

In this approach, precursor particles such as atoms, molecules or nanoparticles assemble and acts as a building block for the formation of complex nanostructures [30]. Sometimes an external driving force is applied to carry out the chemical reaction of these precursor particles. The methods employed in bottom up approach are:

- Chemical vapor deposition (CVD)
- Laser pyrolysis
- Template support synthesis
- Sol-gel processing
- Atomic or molecular condensation
- Plasma or flame spraying synthesis

Sol-gel method:

Sol-gel process helps to synthesize oxide nanostructures and nano powders. It is a versatile soft chemical process. Sol-gel route involves:

1. Hydrolysis
2. Condensation
3. Polymerization
4. Agglomeration

The process involves the conversion of precursors from the “sol” (colloidal) to the “gel” (solid) phase through complex **hydrolysis** and **polycondensation** reactions. This is followed by **calcination** process; drying of the system under different temperatures (below their melting point) to remove the volatile substances and organic compounds. This purification

process is used for the preparation of oxide nano powders [29]. The scheme of sol-gel method is presented in the following Fig3.2.

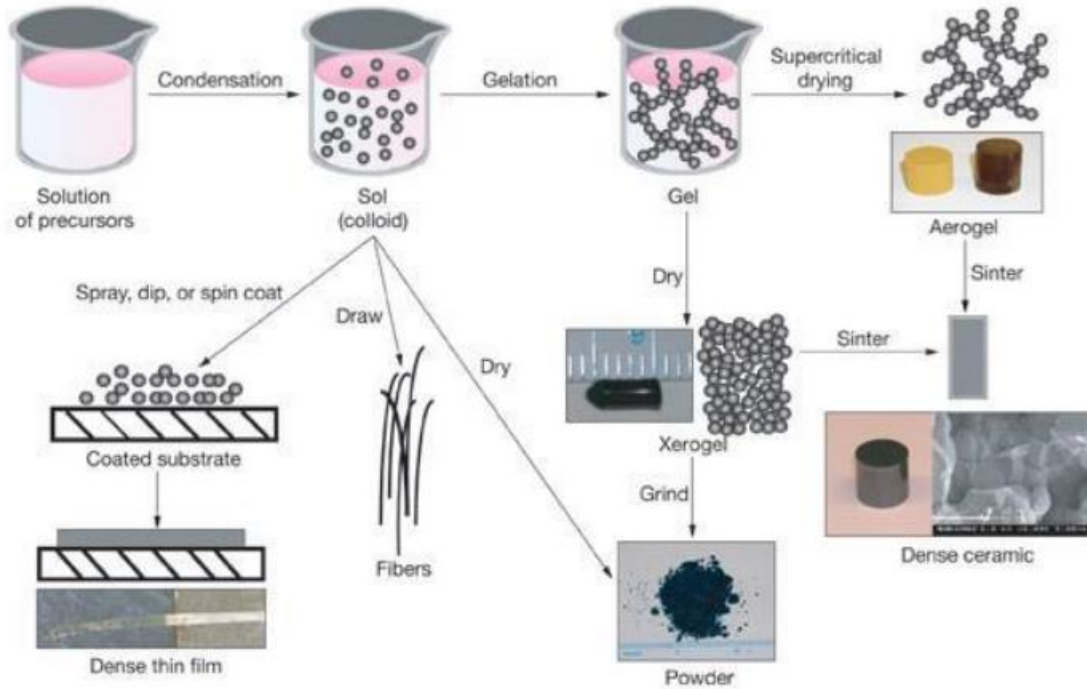


Fig 3.2. Scheme of sol-gel method [29]

Sol gel technique offers several advantages over other methods [29,31] which include:

- Helps in synthesizing nanoparticles at low temperature. This is especially important in processes where substances having low melting point are present.
- Helps to achieve easy shaping and embedding.
- Provides ultra-homogeneous and high purity product.
- By controlling conditions, desired product form such as powders, monolith fibers and films can be obtained.
- It is a very cheap technique for synthesis of nanoparticles.
- It helps to synthesize complex composition materials.

3.2. Characterization techniques for nanoparticles

The techniques used to characterize nanoparticles are:

- Powder X-ray diffraction
- Brunauer-Emmett-Teller Surface area analysis
- Vibrating Sample Magnetometer
- Scanning Electron Microscopy

3.2.1. Powder X-ray diffraction (XRD)

Principle

When X-rays are incident on crystal, diffraction of rays takes place and the pattern of it depends on characteristic structure of crystal. This diffraction pattern is detected by the XRD, providing the information and detection of compounds present in the sample. In case of powder diffraction, X-rays are incident on the powder sample instead of crystal. It is easier and convenient as compared to crystal XRD because it does not require the condition of crystal formation [32].

According to Max Von Laue (1912), crystals behave as 3-D diffraction grating for the X rays having wavelength comparable to the interplanar distance d between planes of the crystal. The cathode ray tube of XRD instrument produces monochromatic and collimated beam of X-ray and is incident on sample. According to Bragg's law, constructive interference occurs upon interaction of these rays with sample. The diffracted rays are counted and a diffractogram is produced; that plots intensity of rays against the angle 2θ [33].

Bragg's law

When X-rays are directed on crystal, they get diffracted by the atoms of the crystals. These rays are partially scattered by upper layer of crystal. The un-scattered ray passes to the next layer and are diffracted by the lower layer (Fig 3.3).

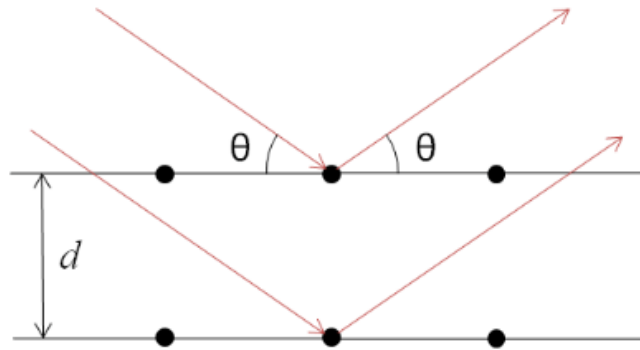


Fig 3.3. Bragg's law

This gives the pattern identical to the one observed by diffraction grating. If the two diffracted beams are in phase, they interfere constructively ultimately giving rise to a diffraction peak in the diffractogram. If the two rays are out of phase, they interfere destructively, and no peak is observed in the diffractogram. Constructive interference takes place only if Bragg's law is obeyed [32]. According to which

$$\sin \theta = \frac{n\lambda}{2d}$$

- θ = incident angle of the X-ray,
- λ = wavelength of X-rays
- d = interplanar distance of atoms.
- n is an integer

Scherrer's Formula

Scherrer's formula is a mathematical relation that is used to find the size of particles of prepared nanoparticles. It gives the relation between particle size and peak width as:

$$t = \frac{0.9\lambda}{\sqrt{B_M^2 - B_s^2 \cos \theta}}$$

- B_s = peak width of a crystalline standard
- λ = wavelength of X-rays,
- θ is the angle of diffraction
- B_M = Width of observed peak

XRD Instrument Working

The XRD instrument consists of following three parts [Fig 3.4]

➤ **X-ray tube:**

It is X-ray source and helps production of X-rays. High voltage provided causes the electron from cathode to move towards anode. These electrons knockout the inner shell electrons of anode metal, causing the electron from outer shell to fall in the inner orbit thereby producing X-rays. Finally, the emitted X-rays are then directed on the specimen.

➤ **Sample stage:**

Sample stage is used to hold the sample under observation. The X-rays from source falls on specimen at angle θ , whereas the detector receives X-rays at angle of 2θ .

➤ **X-ray detector:**

X-ray detector produces electrical signal when it receives X-rays. It counts the number of photons, thus giving the intensity of X-rays reaching the detector [32].

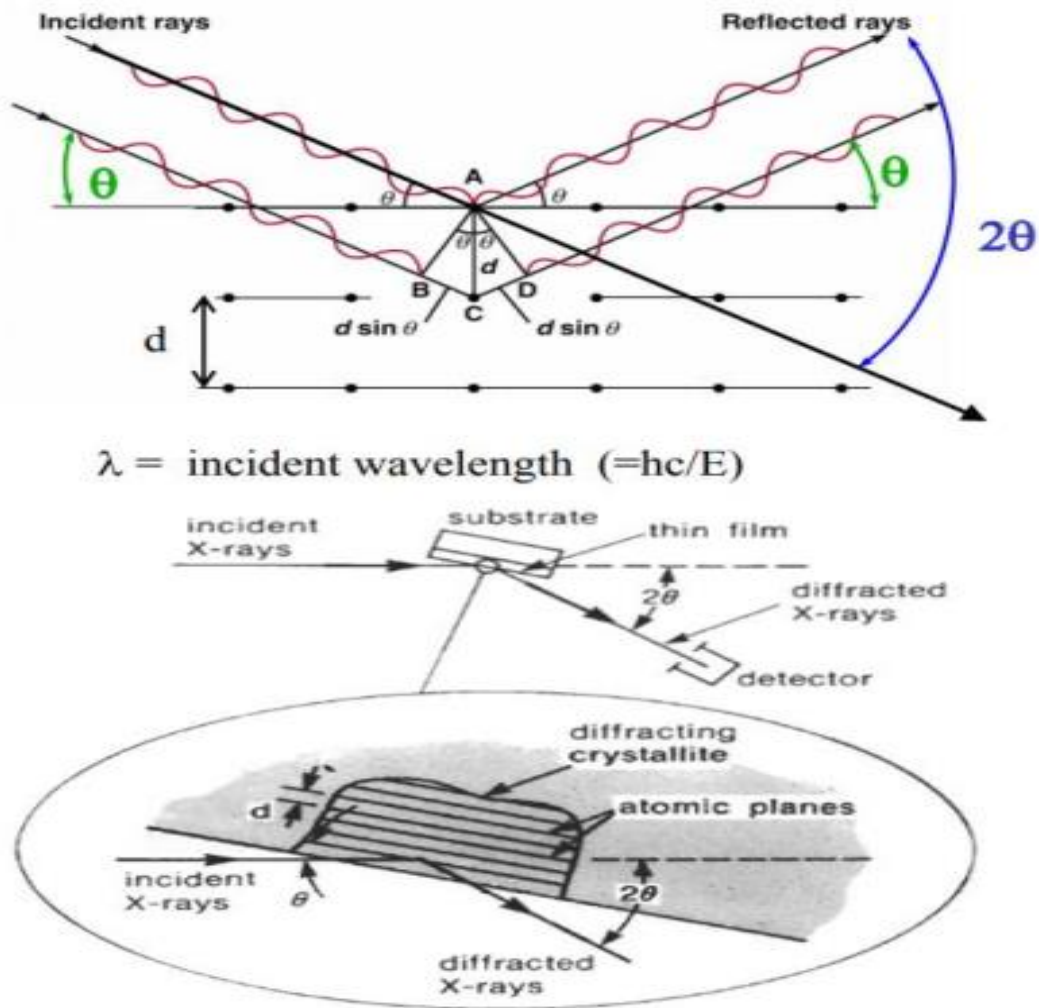


Fig 3.4. Working of XRD instrument [22]

Applications of XRD

XRD is a very useful technique [33] that helps in:

- Identification of compounds present in sample
- Characterization of crystal samples
- Determination of specimen purity
- Identification of crystal structures
- Determination of unit cell parameters.
- Phase identification



Fig 3.5. XRD instrument

3.2.2. Vibrating Sample Magnetometer

VSM was invented in 1955 by Simon Foner to study magnetic properties of sample including remanence, coercivity and intrinsic coercivity. It measures magnetic moment with respect to applied field.

Principle

VSM works on the principle of Faraday's law of induction; the change in magnetic field generates electric field or voltage. The sample is placed between the two electromagnets. The electromagnets generate a uniform magnetic field (H), which causes magnetization (M) in sample. Two sensor coils are also placed around the sample at specific angles. Vibrator made up of linear actuators or modified audio speakers are used to cause sinusoidal motion in the sample by inducing mechanical vibrations in it [Fig 3.6]. Due to the vibrations of sample, magnetic flux in the sample changes inducing voltage in the sensor coils. The induced voltage thus produced is proportional to M . Lock-in amplifier that uses

piezoelectric signal measures the induced voltage in sensing coils. The software converts the change of signal to values giving hysteresis loop; curve of magnetization (M) against the field strength (H) [34].

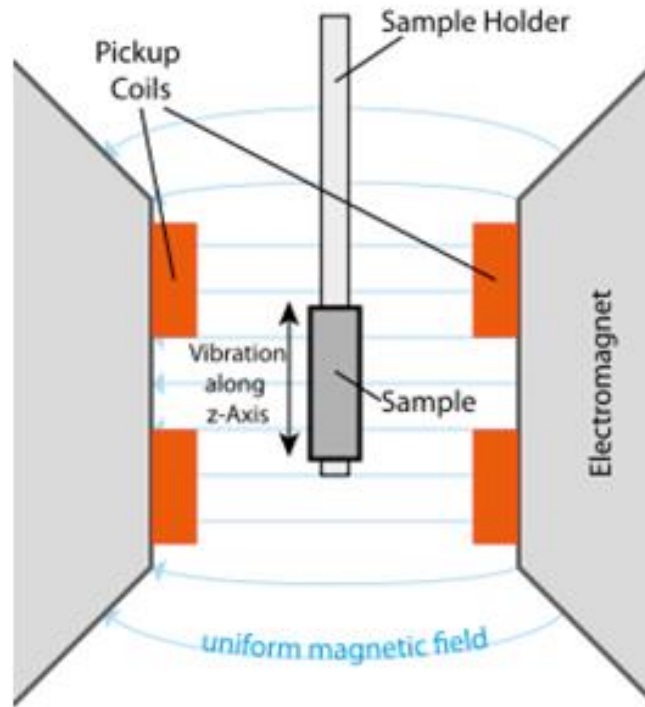


Fig 3.6. VSM mechanism [35]

Parts of VSM

Vibrating Sample Magnetometer consists of following parts:

- Power supply
- Water cooled electromagnets
- Sensor coils
- Reference coils
- Lock-in amplifier
- Vibrator
- Sample holder

- Sample (can be powder, bulk or crystal)

Advantages of VSM

VSM offers following advantages [36]:

- Allows to test the sample at different angles
- Sensitive instrument for magnetic measurements
- It is fast and easy to use
- Provides accurate measurements

3.2.3. Scanning Electron Microscopy (SEM)

The morphological analysis of sample is done using scanning electron microscopy that works by focusing electrons beam on specimen surface.

Principle

The high-energy electron beam (primary electrons) is accelerated towards the anode and possesses significant amount of kinetic energy. The electrons are decelerated upon interaction with atoms of sample specimen. Due to this **Sample-Electron Interaction**, various secondary signals are produced consisting of:

- **Secondary electrons:**

They yield SEM image specially to give topography and morphology of the sample

- **Backscattered electrons:**

They are valuable in giving contrasts of multiphase samples (for rapid phase discrimination).

- **Characteristic X-rays:**

They are used to carry elemental analysis.

- **Diffacted backscattered electron:**

They provide information about structure of crystal.

The mechanism of sample and electron interaction is shown in the following Fig 3.7 [37].

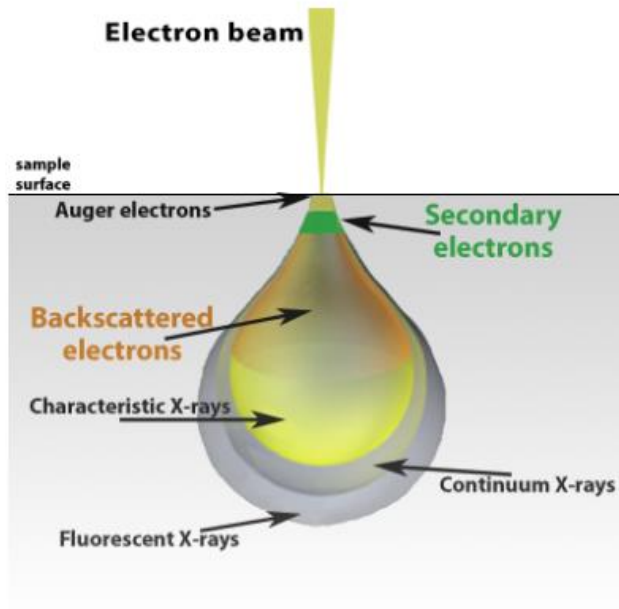


Fig 3.7. Mechanism of sample-electron interaction

Parts and Working

The essential parts of Scanning Electron Microscope (SEM) are [38]:

- **Electron Source ("Electron Gun"):**

Electron source present at top of column generates beam of electrons.

- **Electron lenses:**

The electrons first pass through the **Condenser lens** when they are emitted by the source. Electron beam is directed towards sample specimen by condenser lens and is further converged at sample through **Objective lens**.

- **Sample Chamber:**

The sample under consideration is placed on the sample stage

- **Electron detector:**

The detector constructs the image of sample by detecting the secondary electron and then comparing the intensity of secondary electrons with the primary electrons. Different detectors are used for different type of electrons produced as a result of sample-electron

interaction. In case of secondary electrons (gives morphology of sample), **Everhart-Thornley detector** is used which consists of scintillator. The scintillator accelerates the secondary electrons and convert them into electrical signals, which are then amplified giving 3D-image of the sample

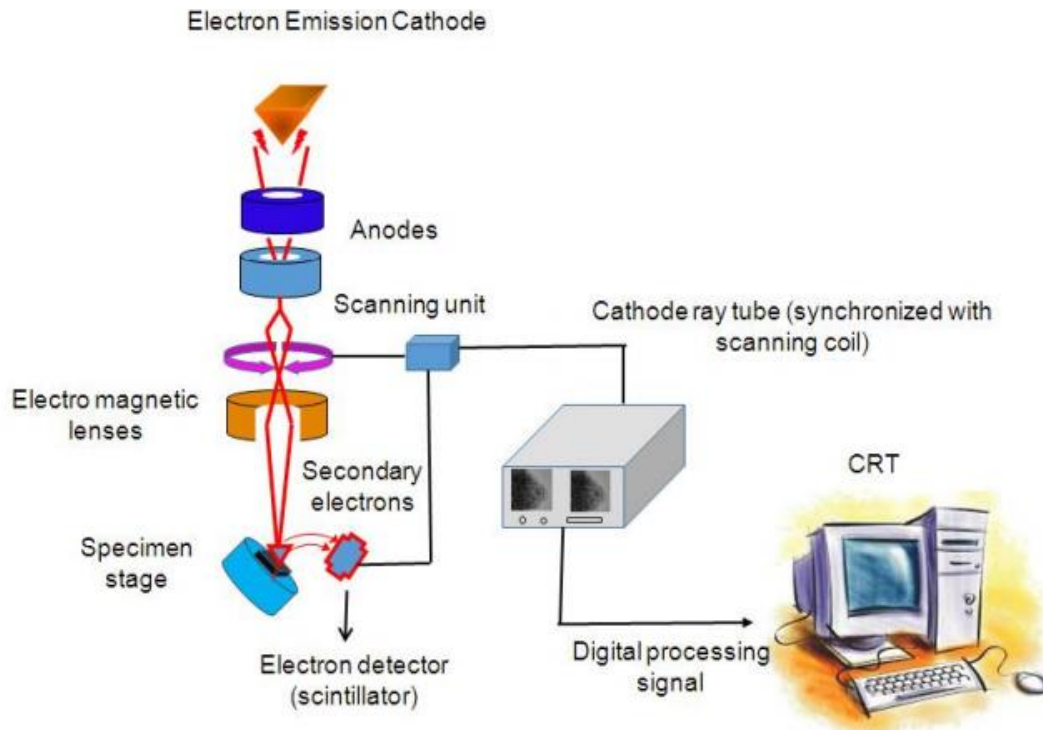


Fig 3.8. Working of SEM [39]

Applications of SEM

- It helps to analyze the gate widths in semiconductor device.
- It helps to observe morphology and topography of the material.
- It helps to discriminate different phases of multiphase sample (for rapid phase discrimination).
- It is used for elemental compositional analysis.
- It is used to examine crystal structure.



Fig 3.9. SEM instrumentation

3.2.4. Brunauer-Emmett-Teller (BET) analysis

BET is named based on three scientists, Stephen Brunauer, Edward Teller and Paul Emmett who developed this method in 1938. BET analysis finds surface area along with distribution of pore size of the sample.

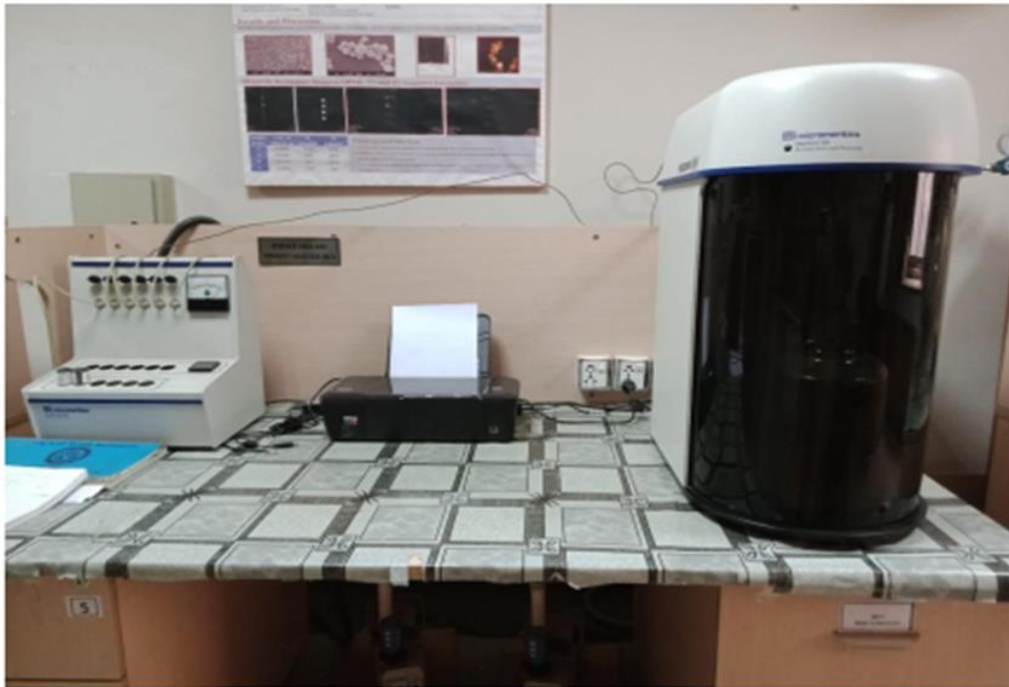


Fig 3.10. BET surface area analyzer

Principle

BET technique works on the principle of gas adsorption. When the subjected gas molecules come in contact with the solid material, the gas gets adsorbed into the solid surface. The amount of the gas adsorbed depends upon the temperature, the kind of gas, gas pressure and the size of the surface area. Any gas that can be physically adsorbed by the solid surfaces and can be desorbed upon decreasing pressure (at same temperature) can be used. However, nitrogen gas is commonly used due to its easy availability in highly pure form. Moreover, it shows strong interaction with the solid surfaces.

The volume of nitrogen gas adsorbed into the solid surface is measured at the B.P of nitrogen (-196°C). As this temperature is less than critical temperature, the gas condenses on the surface. This condensation takes place in the form of monolayer. By using BET equation, the amount of gas adsorbed in the form of a monolayer can be calculated from the isotherms.

As the size of the gas molecules is known, the amount of gas adsorbed by the solid is linked to surface area of particles and pores present at surface [57].

3.3. Synthesis of BFO and BLFMO nanoparticles

BLFMO ($\text{Bi}_{1-x}\text{La}_x\text{Fe}_{1-y}\text{Mn}_y\text{O}_3$) nanoparticles were fabricated by employing double solvent sol-gel method. Other conventional methods i.e. solid-state method to prepare the oxide were avoided because of their high processing temperature which can cause evaporation loss of Bi having relatively low melting point of 934 °C [40]. Thus, Sol-gel method (wet chemical process) that operates on low processing temperature was selected for the preparation of oxide nano-powder. The nanoparticles synthesized were:

- $\text{Bi}_{0.90}\text{La}_{0.10}\text{FeO}_3$ (as BLFO)
- $\text{Bi}_{0.90}\text{La}_{0.10}\text{Fe}_{0.95}\text{Mn}_{0.05}\text{O}_3$ (as BLFMO-5)
- $\text{Bi}_{0.90}\text{La}_{0.10}\text{Fe}_{0.85}\text{Mn}_{0.15}\text{O}_3$ (as BLFMO-15)
- $\text{Bi}_{0.90}\text{La}_{0.10}\text{Fe}_{0.80}\text{Mn}_{0.20}\text{O}_3$ (as BLFMO-20)

3.3.1. Apparatus

The equipment used in the procedure were:

- Magnetic hot plate
- Digital weight balance
- Drying oven
- Muffle furnace
- Mortar and Pestle

3.3.2. Chemical Reagents

Chemical Reagent	Chemical formula
Bismuth-nitrate pentahydrate	$\text{Bi}(\text{NO}_3)_3 \cdot 5\text{H}_2\text{O}$
Lanthanum nitrate hexahydrate	$\text{La}(\text{NO}_3)_3 \cdot 6\text{H}_2\text{O}$
Iron nitrate non-hydrate	$\text{Fe}(\text{NO}_3)_3 \cdot 9\text{H}_2\text{O}$
Manganous nitrate	$\text{Mn}(\text{NO}_3)_2$
Ethylene glycol	$\text{C}_2\text{H}_6\text{O}_2$
Acetic Acid	CH_3COOH

Table 3.1. Chemical Reagents used in synthesis of BLFMO

3.3.3. Procedure

The following procedure was followed for the synthesis of BLFMO:

- Bismuth nitrate pentahydrate & lanthanum nitrate hexahydrate in stoichiometric amounts were dissolved. The resulting mixture was mixed in acetic acid and EG and was stirred for 90 min at 40° C.
- Iron nitrate non-hydrate powders and manganous nitrate was dissolved thoroughly in acetic acid and was stirred for 90 min at 40° C. Constant stirring was ensured throughout this process.
- Above both solutions were mixed together and stirred at 40°C for 180 min.
- The Volatile nature of Bismuth results in its loss during drying process. Excess Bi (3%) was added to compensate for Bi loss during process of heating.
- The obtained solution was oven dried at 80°C for 12h to obtain gel.
- This was followed by calcination process operating at 600°C for 3h. The powder obtained was ground to get fine powder.

The flow chart for BLFMO preparation is presented in Fig 3.11.

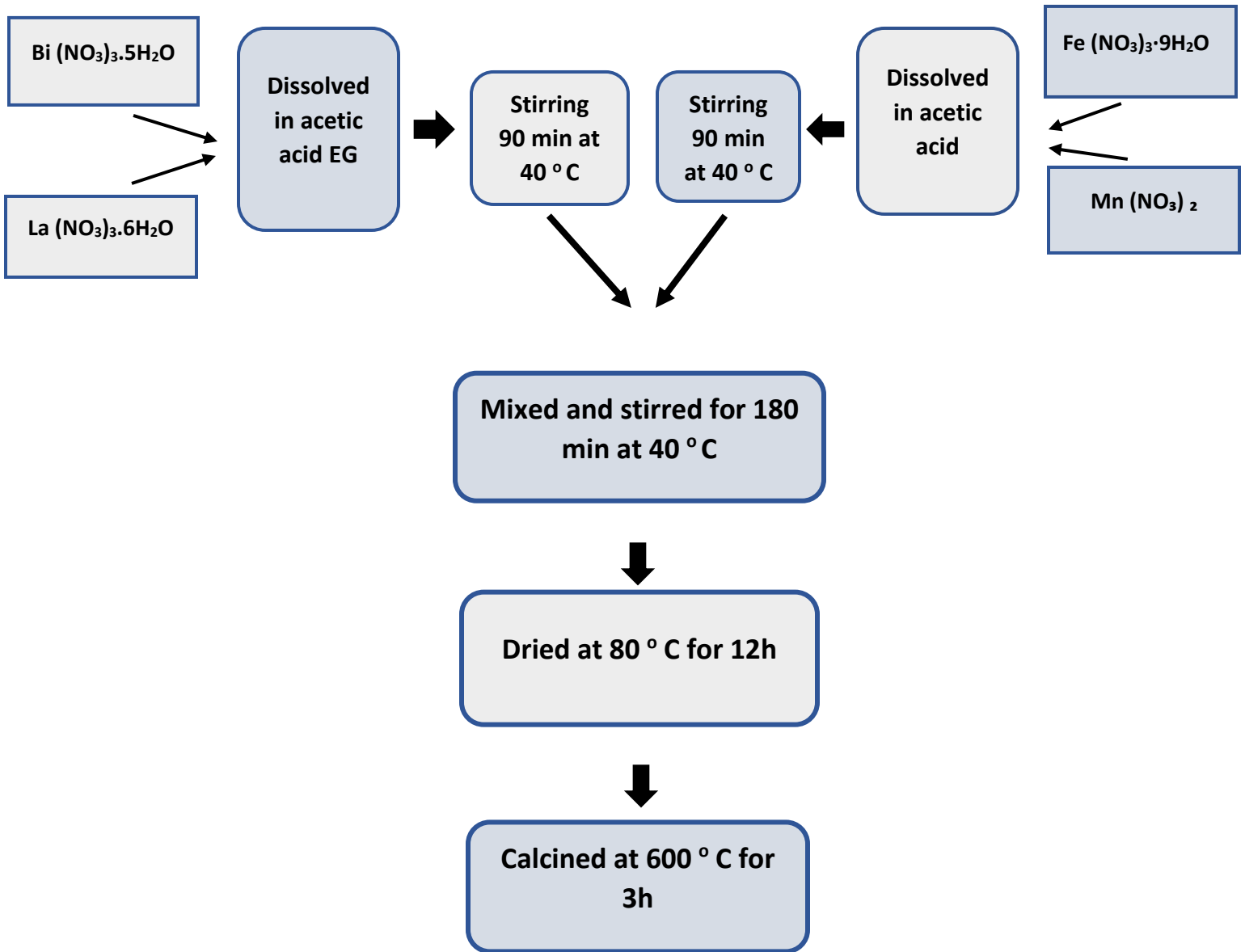


Fig 3.11. Flow chart for BLFMO Synthesis

Double solvent Sol-gel technique

Double solvent Sol-gel is based on **Pechini method** or the **complexation-polymerization reaction** for synthesis of highly homogeneous oxide product due to formation of complex and gel as an intermediate part [41]. It employs two solvents in the process of nanoparticles synthesis i.e. Ethylene glycol ($C_2H_6O_2$) and acetic acid (CH_3COOH).

- **Ethylene glycol (EG):**

Bi and Fe have different electronegativities (Bi has 2.02, Fe has 1.83), due to which they show different hydrolysis rates. Bi is easily hydrolyzed in the solution whereas Fe has slow hydrolysis rate. This makes it difficult to obtain a stable solution and thus the production of ultra-homogeneous product is not possible. Ethylene glycol is an organic carrier and acts as complexing agent for the Bi^{3+} and Fe^{3+} . Ethylene glycol has a linear structure and through complexation-polymerization reaction, it tends to capture the metal ions and stabilize them homogeneously in the matrix. This decreases the mobility of precursors during hydrolysis and tends to minimize the difference in hydrolysis rates. Thus, it helps to obtain a highly stable solution by acting as a template for linearly arranged precursor molecules [42].

Ethylene glycol also helps in preventing the agglomeration of nanoparticles. This is also due to its ability to form complex with heterometallic ions hindering their segregation. Hence, it acts as a stabilizer to prevent precipitation and agglomeration of the metal ions [24].

In both the ways discussed above, Ethylene glycol helps to obtain ultra-homogeneity that is essential for oxide preparation.

- **Acetic acid:**

Iron can exist in the form of Fe^{+3} or Fe^{+2} due to which it can precipitate in the form of insoluble products such as Ferric hydroxide. The precipitation reaction is most favorable when the water amount is decreased during the heating and drying process. This precipitation

of salts effects the homogeneity of product. In order to prevent the precipitation, chelating agent like acetic acid is used. Acetic acid acts as a catalyst and takes up Iron to form soluble complexes. Acetic acid maintains the hydrolysis speed and adjusts the solution concentration [42,43].

Chapter 4

Results and Discussion

4.1. X-Ray Diffraction analysis

XRD was utilized to analyze the phase purity of the formation. XRD was performed using a Rigaku 2500 X-ray diffractometer with Cu-K α radiation source ($\lambda = 0.1542$ nm). The XRD pattern for the pure BFO, Lanthanum doped BFO and Lanthanum and Manganese co-doped BFO is shown in the Fig4.1. All the observed diffraction peaks can be indexed as rhombohedral phase of BiFeO₃ according to JCPDS card no. 71-2494

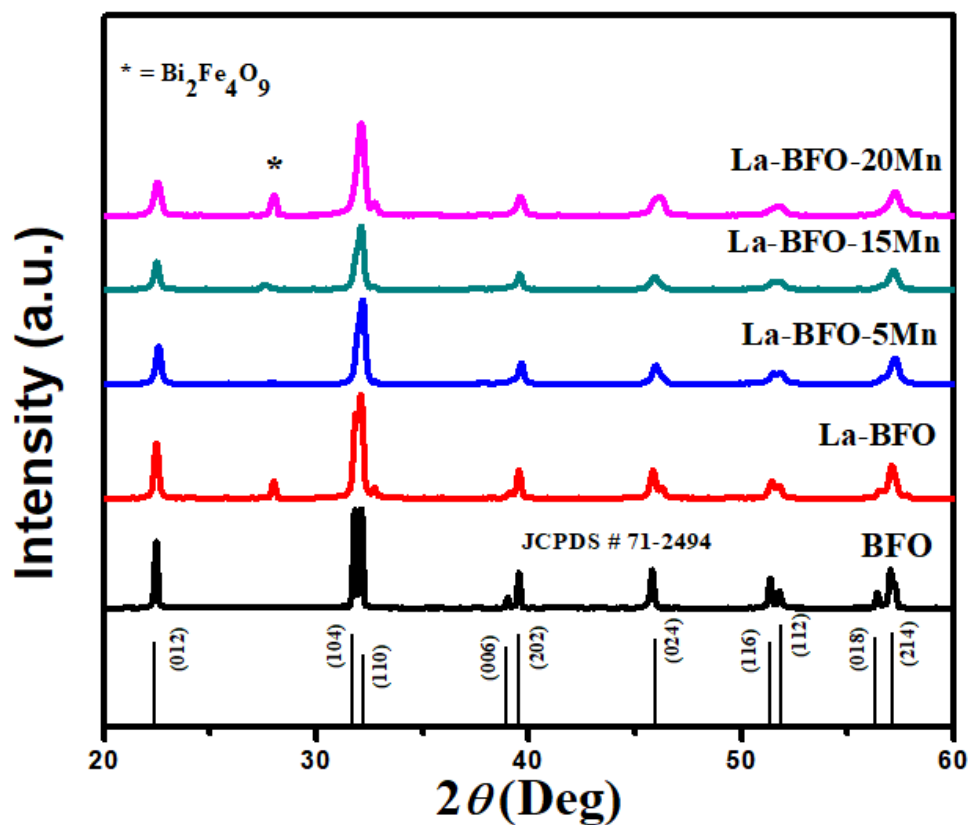


Fig4.1. XRD for BFO, BLFO-(10%) and BLFMO-(5,15,20%) at room temperature

Peaks (006), (202), (018), (104) and (110) are of extreme importance. In XRD data, by comparing the peaks of BFO, BLFO and BLFMO it is clearly observed that the (006) and (018) diffraction peaks diminish by adding dopant in the BFO and tends to disappear completely when the Mn concentration is increased to 20%. Similarly, the intensity of the peak (202) is found to be decreasing with the increase in Mn concentration [44]. These results can be explained based on the phase transition from rhombohedral to orthorhombic caused by doping, as observed in other reports [45,46].

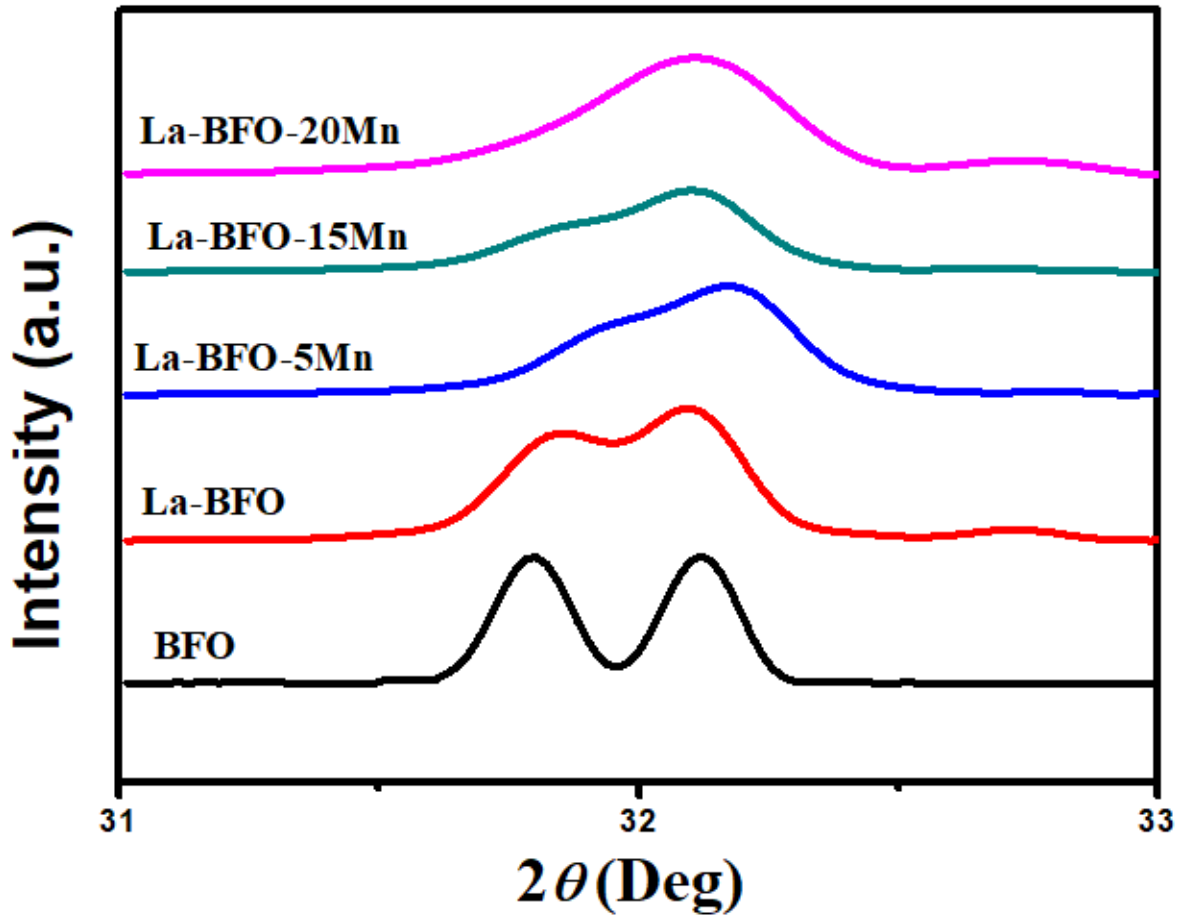


Fig4.2. Bragg peak shift in BLFMO

Fig4.2 shows that (104) and (110) peaks are clearly separated in the pure BFO. However, by increasing the dopant concentration in BFO, (104) and (110) twin Bragg-peak

is slowly merging towards a single diffraction peak. A similar type of phenomenon was also observed in other studies [47]. Also, this BLFMO merged peak is shifting to higher angle as compared to pure BFO sample. This phenomenon can be attributed to the fact that there is an ionic radius mismatch between dopant and the host cation. Dopant ion Mn^{+2} has lower ionic radius (0.645 \AA) as compared to the host Fe^{+3} (0.782 \AA) ion. When Mn^{+2} is substituted at Fe^{+3} site, lattice strain is induced inside the lattice [26]. The increase in lattice strain is also evident from Table 4.1 as calculated by Scherrer's formula. This lattice strain decreases the lattice parameters (a and c) and interplanar distance (d) resulting in the Bragg peak shift towards higher angle [47]. This is according to Bragg's law:

$$2d\sin\theta = n\lambda$$

$$\sin\theta = n\lambda / 2d$$

Samples	Lattice strain
BFO	0.08%
BLFO	0.183%
BLFMO-5	0.264%
BLFMO-15	0.278%
BLFMO-20	0.343%

Table 4.1. Lattice strain calculated by Scherrer's formula

All these findings are in good agreement with the literature [27]. These results overall suggest that La and Mn doping causes lattice distortion and thus leads to rhombohedral to orthorhombic phase transition [48]. From Scherrer's formula, the crystallite size is calculated and is found to be decreasing from BFO (84nm) to BLFMO (34nm). This can be ascribed to the fact that the mismatch of the dopant and the host ionic radii decreases the rate of the

nucleation and hence restricts its growth, ultimately causing the reduction in crystallite size [47].

XRD data shows that no 2nd phase (impurity) is observed in BLFMO-5. However, a small intensity peak of 2nd phase Bi₂Fe₄O₉ is detected in BFLMO-15 and its intensity is increased in case of BFLMO-20. This suggests that the increased concentration of Mn⁺² is responsible for formation of this 2nd phase. It can be explained on the basis that when concentration of Mn⁺² is increased, the unbalanced charge is neutralized by the process of charge compensation; creating more cation vacancies rather than suppressing oxygen vacancies. The driven out Bi atoms in this process go on to form bismuth rich phases like Bi₂Fe₄O₉ [49]

4.2. Vibrating Sample magnetometer (VSM)

In order to study the magnetic properties of pure BFO, La doped BFO (BLFO) and La and Mn co-doped BFO (BLFMO-5, BLFMO-15, BLFMO-20), VSM was performed. Magnetization vs. magnetic field (M-H) loop for the samples are presented in Fig4.3

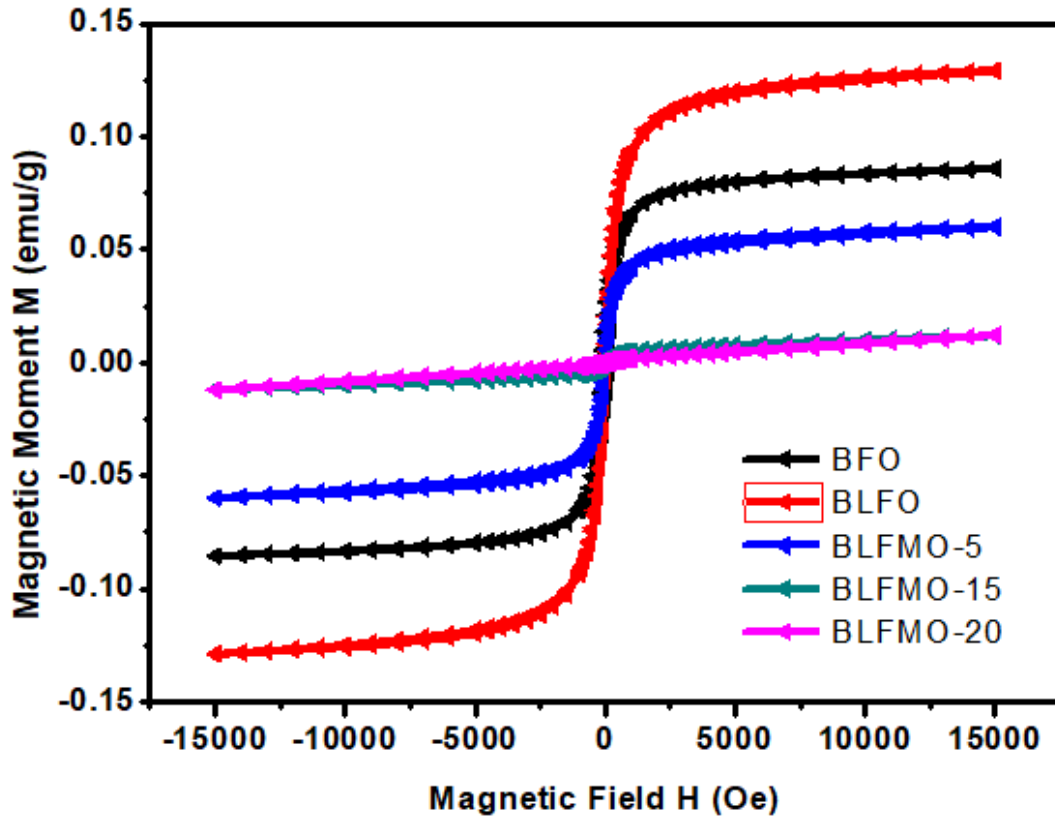


Fig4.3. M-H loops for BFO, BLFO (10%) and BLFMO-(5,15,20%) at room temperature

4.2.1. Saturation Magnetization (M_s):

The lanthanum doped BFO shows increase in saturation magnetization (M_s) as compared to pure BFO. Whereas saturation magnetization decreases with an increase in concentration of manganese dopant as demonstrated in Table4.2 and Fig4.4.

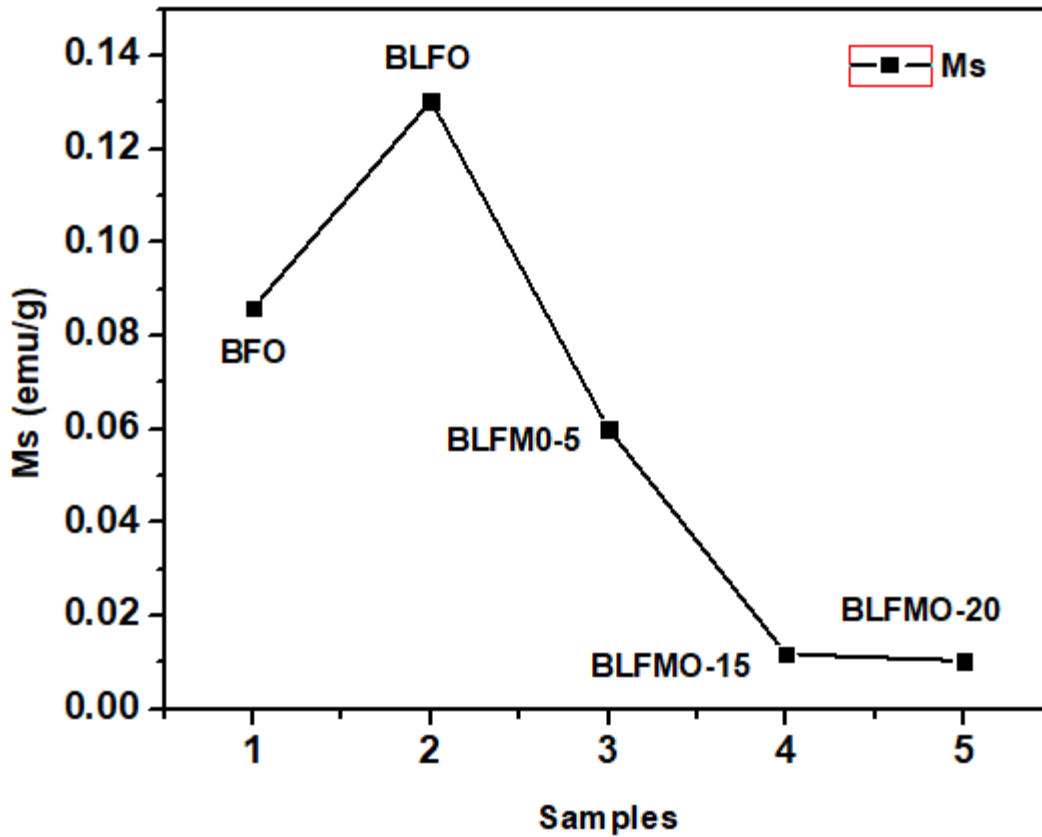


Fig4.4. Saturation magnetization vs pure and doped BFO

Pure BFO in bulk is antiferromagnetic with G type spin having a spiral spin structure of 62nm. The spin orbit interactions produces spin canting leading to imperfect anti-ferromagnetic nature of BFO. This spin canting produces small moments causing weak magnetism in BFO [21]. In our results, pure BFO does not exhibit macroscopic magnetization, consistent with previous reports [50,51]. The increase in saturation magnetization value from 0.0859 emu/g to 0.1304 emu/g when fixed amount of lanthanum (0.10) is doped can be ascribed to the suppression of the spin modeling structure caused by lanthanum substitution at A site in BFO. This is in line with the previous work that reported the collapse of spin cycloid structure of BFO upon lanthanum doping significantly improves the multiferroic properties of BFO [52, 20]. This collapse of spin structure is found to be

caused by the lanthanum due to the fact that its doping causes phase transition from rhombohedral to orthorhombic in BFO. This phase transition releases the locked magnetization in spin cycloid structure leading to enhanced saturation magnetization [53].

Samples	M_r (emu/g)	M_s (emu/g)	H_c (Oe)	M_r/M_s	H_{EB}
BFO	0.0208	0.0859	126.53	0.2421	4
BLFO	0.0080	0.1304	31.73	0.0617	1
BLFMO-5	0.0016	0.0601	9.64	0.0272	3
BLFMO-15	0.0006	0.0118	41.82	0.0567	6
BLFMO-20	0.0005	0.0105	124.56	0.0479	41

Table 4.2. Magnetic parameters of pure and doped BFO extracted from Fig 4.3

Table4.2. shows the decrease in magnetization value from 0.061 emu/g to 0.0105 emu/g as the percentage of Manganese dopant is increased from 5% to 20% keeping the lanthanum fixed (10%). These values are much less as compared to the pure BFO and lanthanum doped BFO. This decreased magnetization can be related to the super exchange effect. Mn⁺² and Fe⁺³ consists of partially filled d orbitals whereas oxygen consists of filled p orbital. The electrons from this p orbital of oxygen are coupled to both the cations having half-filled orbitals as shown in the Fig4.5.

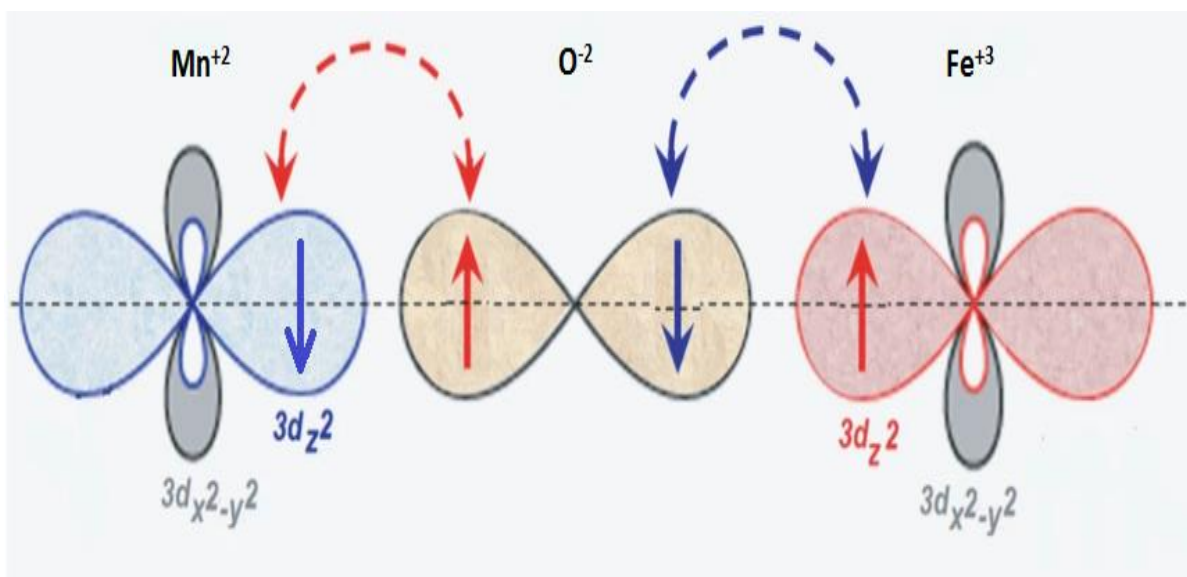


Fig4.5. Super-exchange effect between Fe^{+3} and Mn^{+2}

This results in the antiferromagnetic coupling between the doped Mn^{+2} with the host Fe^{+3} ions as proposed by the Goodenough Kanamori rules [54]. This 180° cation-anion-cation interaction between Fe^{+3} and Mn^{+2} with oxygen as nonmagnetic anion between them is producing weak magnetism in Mn doped BFO [55]. This interaction occurs at the octahedral sites of BFLMO. The similar type of result is observed in previous study [56]. It is observed that saturation magnetization is decreasing with increase in the concentration of Mn dopant. It is due to the fact that more Mn substitution enhances the super-exchange effect due to increased coupling. Thus, giving BFLMO antiferromagnetic nature.

4.2.2. Coercivity

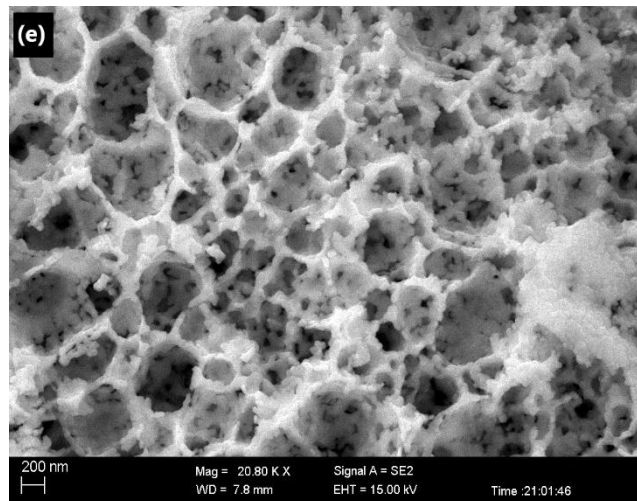
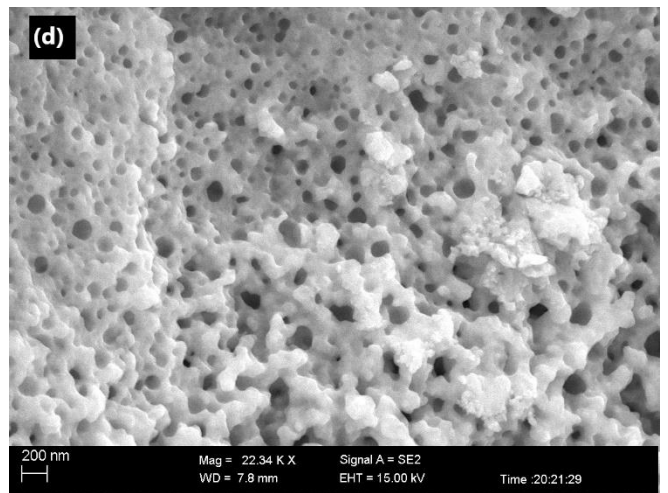
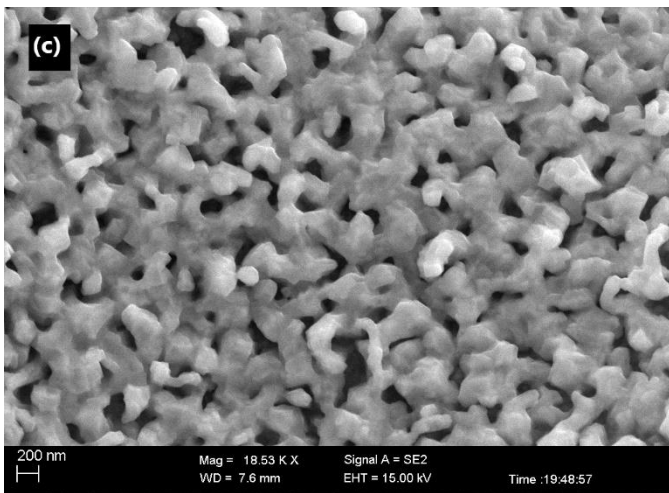
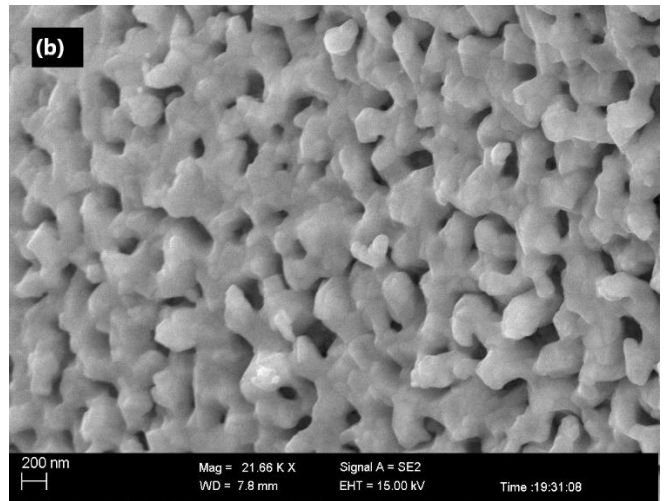
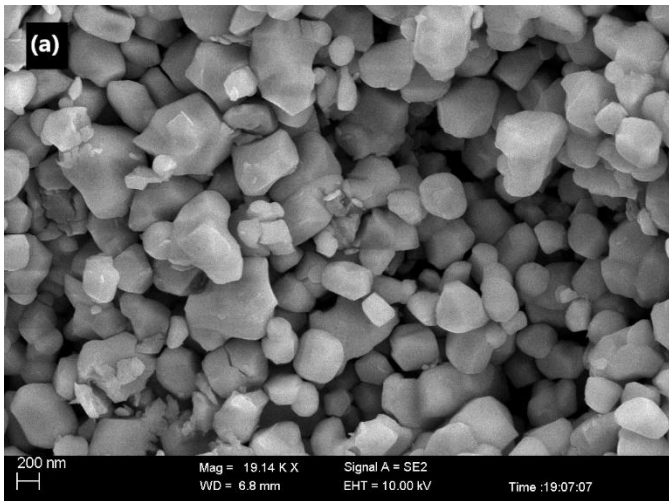
The coercivity is found to be decreasing in case of BLFO, BLFMO-5 and BLFMO-15 as evident from Table 4.2. However, in BLFMO-20 the coercivity value is increased which can be ascribed to the increase in magnetic anisotropy when Mn^{+2} concentration is increased to 20%. The increase in coercivity suggests that BLFMO-20 is moving towards hard magnet.

Moreover, the presence of exchange bias phenomenon in BLFMO-20 sample also supports the presence of antiferromagnetic phase in sample.

The VSM results overall suggests that the ferromagnetism in BFO is enhanced by La doping whereas the Mn doping leads to the formation of antiferromagnetic phase. Thus, both ferromagnetic and antiferromagnetic phases can be achieved within same material by co-doping BFO with La and Mn simultaneously. This makes BLFMO suitable for both hard and soft magnetic applications.

4.3. Scanning Electron Microscopy (SEM)

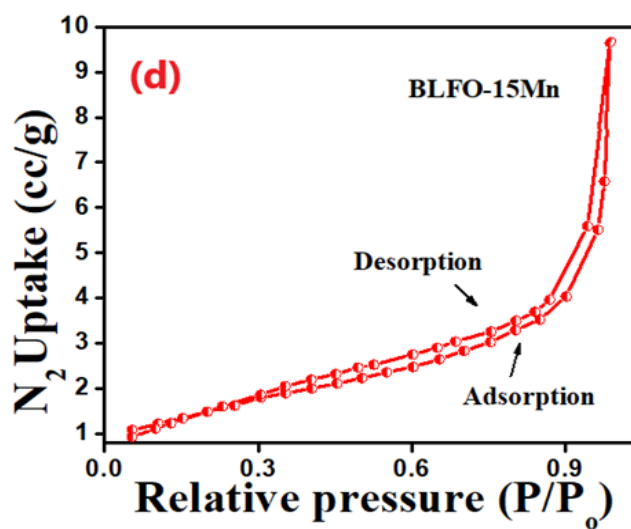
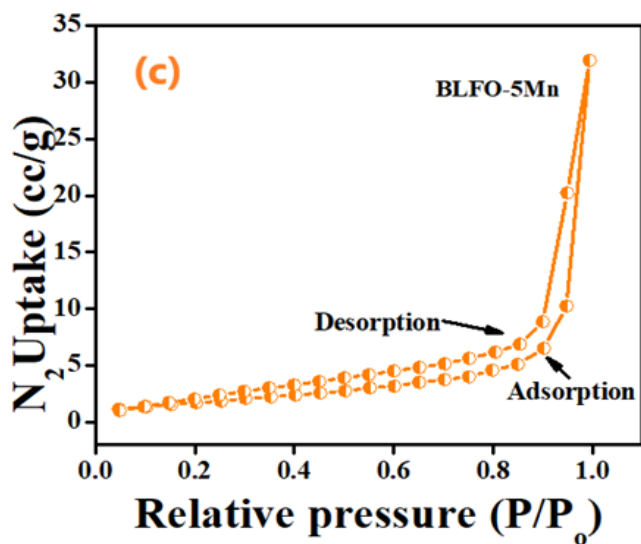
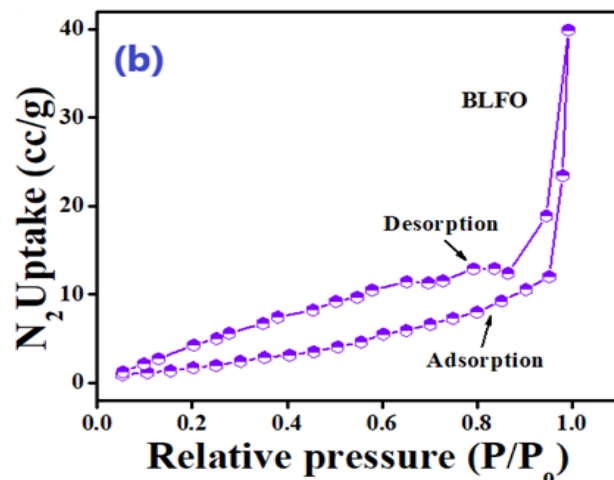
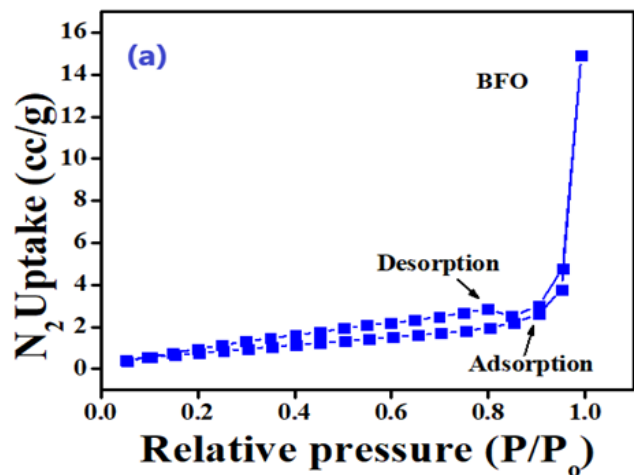
Morphological analysis of pure sample and doped BFO was done by SEM. Fig 4.6. shows SEM images of BFO and various BLFMO nanostructures. SEM micrographs of BLFO and BLFMO-5 (Fig 4.6. b & c) clearly indicates the formation of a well-ordered mesoporous network structure with ordered porosity. Whereas, when the concentration of Mn dopant is increased in case of BLFMO-15 and BLFMO-20 (Fig 4.6. d & e), the network structure starts degrading and the ordered porosity is lost. This is explained in terms of different ionic radii of substituent and host cations which leads to structural distortions and ultimately decrease in cell volume. The reduction in cell volume decreases the nucleation rate and hence the grain growth is reduced [47]



4.6. SEM images of (a) pure BFO sample (b) BLFO (c) BLFMO-5% (d) BLFMO-15% (e) BLFMO-20%

4.4. BET Analysis

BET was performed to find the pore size and surface area of prepared samples. N_2 adsorption-desorption isotherms of BFO, BLFO, BLFMO-5, BLFMO-15 and BLFMO-20 are presented below (Fig 4.7).



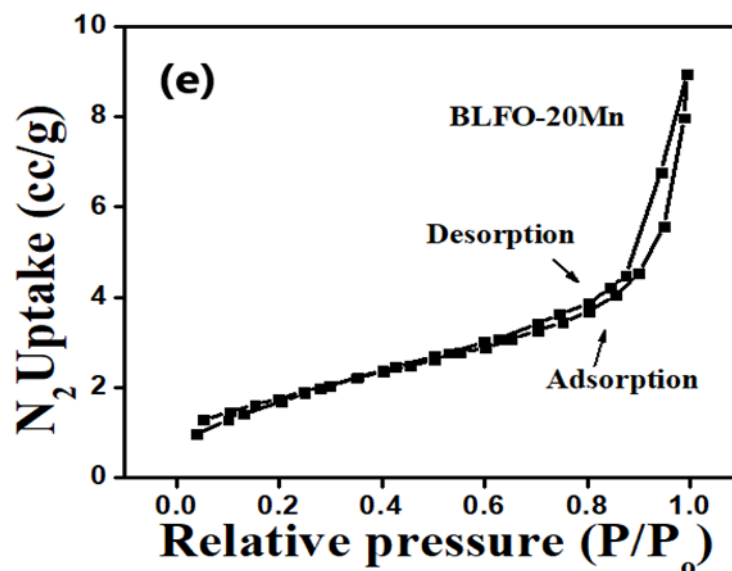


Fig 4.7. N₂ gas isotherms of (a) BFO sample (b) BLFO (c) BLFMO-5% (d) BLFMO-15% (e) BLFMO-20% measured at 77K

The N₂ gas isotherms of all the samples demonstrate typical type II isotherms. The pore size and surface area of all the nanostructures are presented in Table 4.3. The narrow hysteresis curves and the pore size values of all samples indicate the presence of mesopores in prepared nanoparticles. BET results suggest that mesoporous nanostructures are successfully fabricated without using any template.

Samples	Surface area (m ² /g)	Pore size (nm)
BFO	3.3	2.2
BLFO	5.8	2.5
BLFMO-5	9.0	3.5
BLFMO-15	6.8	2.5
BLFMO-20	7.7	2.2

Table 4.3. Surface area and pore size of various BFO nanostructures extracted from BET.

Conclusion

In conclusion, this research presents a simple and easy template-free method for the fabrication of mesoporous gyroidal nanostructures. This approach helps in the preparation of mesoporous nanostructures through a simple and low-cost technique for commercial applications. This approach for synthesis has advantages over several other template methods which require complicated procedure, are expensive and can lead to contamination and toxicity. Moreover, the selection of nontoxic, inexpensive and stable template makes other methods really challenging.

XRD results suggested that phase transition from rhombohedral to orthorhombic takes place upon La and Mn co-doping. This transition occurs due to structural distortions caused by host and dopant ionic radii mismatch.

Scanning Electron microscopy indicated the presence of a well ordered mesoporous gyroidal nanostructures in BLFO and BLFMO-5. However, with the increment in Mn concentration (BLFMO-15 and BLFMO-20), the ordered porosity is lost, and network started degrading.

VSM study revealed the enhanced ferromagnetism caused by La doping which can be attributed to the disruption of spin cycloid structure of BFO, releasing locked magnetization. However, Mn doping leads to the formation of antiferromagnetic phase in BFO nanostructures. Thus, the prepared co-doped BFO nanoparticles exhibit both ferromagnetic and antiferromagnetic phases within same material. These results suggest that co-doped BFO nanostructures are potential candidates for both soft and hard magnetic applications.

References

- [1] 2005, Written by AZoNanoJun 27. “Nanoscience - What Is Nanoscience and What Will Its Impact Be?” *AZoNano.com*, 31 July 2017, www.azonano.com/article.aspx?ArticleID=1282.
- [2] “History of Nanotechnology.” *Trynano.org*, 25 June 2018, www.trynano.org/about/history-nanotechnology.
- [3] “Nanomaterials.” *National Institute of Environmental Health Sciences*, U.S. Department of Health and Human Services, www.niehs.nih.gov/health/topics/agents/sya-nano/index.cfm.
- [4] *What Is a Nanomaterial?*, www.safenano.org/knowledgebase/resources/faqs/what-is-a-nanomaterial/.
- [5] Author. “Global Research and Analytics Firm.” *Aranca*, Aranca, 4 Dec. 2015, www.aranca.com/knowledge-library/infographics/ip-research/types-of-prevalent-nanoparticles.
- [6] U.S. Environmental Protection AgencyMar. “Classification of Nanomaterials, The Four Main Types of Intentionally Produced Nanomaterials.” *AZoNano.com*, 31 July 2017, www.azonano.com/article.aspx?ArticleID=1872.
- [7] <https://shodhganga.inflibnet.ac.in/bitstream/10603/119265/3/chapter%20i.pdf>.
- [8] Han, Jie, et al. “Fundamentals of Nanomaterials.” *Nano Letters*, vol. 7, no. 12, 2012, pp. 24611–17, doi:10.1039/c1cc13658e.

- [9] shodhganga.inflibnet.ac.in/bitstream/10603/119265/3/chapter%20i.pdf.
- [10] “What Is Nanoscience?” *INA*, ina.unizar.es/the-institute/what-is-nanoscience/.
- [11] Lichtarowicz, Marek. *Nanomaterials*, www.essentialchemicalindustry.org/materials-and-applications/nanomaterials.html.
- [12] *What Is Nanoscience? – INA – Instituto De Nanociencia De ...* ina.unizar.es/the-institute/what-is-nanoscience/.
- [13] shodhganga.inflibnet.ac.in/bitstream/10603/48048/11/11_chapter%201.pdf.
- [14] Anonymous. “Multiferroic Surprise.” *Physics*, American Physical Society, 18 Aug. 2015, physics.aps.org/synopsis-for/10.1103/PhysRevLett.115.087601.
- [15] *Complex Oxide Superstructures & Emergent Phenomena Research Group*, info.phys.tsinghua.edu.cn/yupu/research.html.
- [16] Irfan, Syed, et al. “Mesoporous Template-Free Gyroid-like Nanostructures Based on La and Mn Co-Doped Bismuth Ferrites with Improved Photocatalytic Activity.” *RSC Advances*, vol. 6, no. 115, 2016, pp. 114183–89, doi:10.1039/c6ra23674j.
- [17] Chauhan, Sunil, et al. “Structural, Vibrational, Optical, Magnetic and Dielectric Properties of Bi_{1-x}BaxFeO₃ Nanoparticles.” *Ceramics International*, vol. 39, no. 6, Elsevier, 2013, pp. 6399–405, doi:10.1016/j.ceramint.2013.01.066.
- [18] Cheng, Z. X., et al. “Structure, Ferroelectric Properties, and Magnetic Properties of the La-Doped Bismuth Ferrite.” *Journal of Applied Physics*, vol. 103, no. 7, 2008, pp. 137–40, doi:10.1063/1.2839325.

- [19] Xu, Jia Huan, et al. “Low-Temperature Synthesis of BiFeO₃ Nanopowders via a Sol-Gel Method.” *Journal of Alloys and Compounds*, vol. 472, no. 1–2, 2009, pp. 473–77, doi:10.1016/j.jallcom.2008.04.090.
- [20] Zhang, Shan Tao, et al. “Substitution-Induced Phase Transition and Enhanced Multiferroic Properties of Bi_{1-x}La_xFeO₃ Ceramics.” *Applied Physics Letters*, vol. 88, no. 16, 2006, pp. 200–03, doi:10.1063/1.2195927.
- [21] Park, Tae-jin, et al. *Size-Dependent Magnetic Properties of Nanoparticles*. 2007.
- [22] Mukherjee, A., et al. “Enhancement of Multiferroic Properties of Nanocrystalline BiFeO₃ Powder by Gd-Doping.” *Journal of Alloys and Compounds*, vol. 598, Elsevier B.V., 2014, pp. 142–50, doi:10.1016/j.jallcom.2014.01.245.
- [23] Chen, Zhiwu, et al. “Low-Temperature Preparation of Lanthanum-Doped BiFeO₃ Crystallites by a Sol-Gel-Hydrothermal Method.” *Ceramics International*, vol. 37, no. 7, 2011, pp. 2359–64, doi:10.1016/j.ceramint.2011.03.081.
- [24] Lee, S. J., et al. “Powder Synthesis of Barium Titanate and Barium Orthotitanate via an Ethylene Glycol Complex Polymerization Route.” *Journal of Materials Research*, vol. 14, no. 7, 1999, pp. 3001–06, doi:10.1557/JMR.1999.0403.
- [25] Chauhan, Sunil, et al. “Multiferroic, Magnetolectric and Optical Properties of Mn Doped BiFeO₃ Nanoparticles.” *Solid State Communications*, vol. 152, no. 6, Elsevier Ltd, 2012, pp. 525–29, doi:10.1016/j.ssc.2011.12.037.
- [26] Gupta, Surbhi, et al. “Piezoresponse Force Microscopy and Vibrating Sample Magnetometer Study of Single Phased Mn Induced Multiferroic BiFeO₃ Thin Film.” *Journal of Applied Physics*, vol. 111, no. 6, 2012, pp. 0–6, doi:10.1063/1.3699021.

- [27] Arya, G. S., and N. S. Negi. "Effect of in and Mn Co-Doping on Structural, Magnetic and Dielectric Properties of BiFeO₃ Nanoparticles." *Journal of Physics D: Applied Physics*, vol. 46, no. 9, 2013, doi:10.1088/0022-3727/46/9/095004.
- [28] Garcia, F. Gonzalez, C. S. Riccardi, and Alexandre Zirpoli Simões. "Lanthanum doped BiFeO₃ powders: Syntheses and characterization." *Journal of Alloys and Compounds* 501.1 (2010): 25-29.
- [29] Arole, V. M., and S. V Munde. "Fabrication of Nanomaterials Top-Down and Bottom-Up Approaches - An Overview." *JAAST:Material Science (Special Issue)*, vol. 1, no. 2, 2014, pp. 2–89.
- [30] 2004, Written by AZoNanoDec 14. "Bottom-Up Methods for Making Nanotechnology Products." *AZoNano.com*, 15 Aug. 2019, www.azonano.com/article.aspx?ArticleID=1079.
- [31] Sharma, M., et al. "The Sol-Gel Method: Pathway to Ultrapure and Homogeneous Mixed Metal Oxide Nanoparticles." *Asian Journal of Chemistry*, vol. 30, no. 7, 2018, pp. 1405–12, doi:10.14233/ajchem.2018.20845.
- [32] Libretexts. "Powder X-Ray Diffraction." *Chemistry LibreTexts*, Libretexts, 5 Dec. 2019, [chem.libretexts.org/Bookshelves/Analytical_Chemistry/Supplemental_Modules_\(Analytical_Chemistry\)/Instrumental_Analysis/Diffraction_Scattering_Techniques/Powder_X-ray_Diffraction](http://chem.libretexts.org/Bookshelves/Analytical_Chemistry/Supplemental_Modules_(Analytical_Chemistry)/Instrumental_Analysis/Diffraction_Scattering_Techniques/Powder_X-ray_Diffraction).
- [33] "X-Ray Powder Diffraction (XRD)." *Techniques*, 14 Feb. 2020, serc.carleton.edu/research_education/geochemsheets/techniques/XRD.html.
- [34] *Theory of Operation for VSM - WEISTRON*. www.weistron.com/vsm-theory/

- [35] "Physics - Characterization of Materials." *NPTEL*, nptel.ac.in/courses/115103030/30.
- [36] "Vibrating Sample Magnetometer (VSM)." *Vibrating Sample Magnetometer (VSM), Magnetic Moment Measurement, Magnetic Coercivity Measurement - MicroSense, LLC*, www.microsense.net/products-vsm.htm.
- [37] "Scanning Electron Microscopy." *Nanoscience Instruments*, www.nanoscience.com/techniques/scanning-electron-microscopy/.
- [38] Nanakoudis, Antonis. "What Is SEM? Scanning Electron Microscopy Explained." *Accelerating Microscopy*, 14 Nov. 2019, blog.phenom-world.com/what-is-sem.
- [39] shodhganga.inflibnet.ac.in/bitstream/10603/48048/11/11_chapter%201.pdf.
- [40] Sunde, Tor Olav Løveng et al. "Modified Pechini Synthesis of Oxide Powders and Thin Films." (2016).
- [41] eng.thesaurus.rusnano.com/wiki/article2075.
- [42] <file:///F:/All%20Folder/research%20papers/BFO%20structure%20and%20properties/15%20reference.pdf>.
- [43] *Chelating Agent - Schlumberger Oilfield Glossary*. www.glossary.oilfield.slb.com/en/Terms/c/chelating_agent.aspx.
- [44] Palai, R., et al. " β phase and γ - β metal-insulator transition in multiferroic Bi Fe O 3." *Physical Review B* 77.1 (2008): 014110.

- [45] Guo, Renqing, et al. "Enhanced photocatalytic activity and ferromagnetism in Gd doped BiFeO₃ nanoparticles." *The Journal of Physical Chemistry C* 114.49 (2010): 21390-21396.
- [46] Mukherjee, A., et al. "Enhancement of multiferroic properties of nanocrystalline BiFeO₃ powder by Gd-doping." *Journal of Alloys and Compounds* 598 (2014): 142-150.
- [47] Irfan, Syed, et al. "Enhanced Photocatalytic Activity of La³⁺ and Se⁴⁺ Co-Doped Bismuth Ferrite Nanostructures." *Journal of Materials Chemistry A*, vol. 5, no. 22, Royal Society of Chemistry, 2017, pp. 11143–51, doi:10.1039/c7ta01847a.
- [48] Chauhan, Sunil, et al. "Multiferroic, Magnetoelectric and Optical Properties of Mn Doped BiFeO₃ Nanoparticles." *Solid State Communications*, vol. 152, no. 6, Elsevier Ltd, 2012, pp. 525–29, doi:10.1016/j.ssc.2011.12.037.
- [49] Usama, Hasan M., et al. "Structural Transition and Its Effect in La, Zr Co-Substituted Mono-Domain BiFeO₃." *Journal of Applied Physics*, vol. 120, no. 21, 2016, doi:10.1063/1.4969047.
- [50] Pradhan, A. K., et al. "Magnetic and Electrical Properties of Single-Phase Multiferroic BiFeO₃." *Journal of Applied Physics*, vol. 97, no. 9, 2005, doi:10.1063/1.1881775.
- [51] Composed, Ferroelectric Ferromagnet, and Solid Solution. *A Ferroelectric Ferromagnet Composed Of*. no. 7, 2001, pp. 487–90.

- [52] Chen, Zhiwu, et al. "Low-Temperature Preparation of Lanthanum-Doped BiFeO₃ Crystallites by a Sol-Gel-Hydrothermal Method." *Ceramics International*, vol. 37, no. 7, 2011, pp. 2359–64, doi:10.1016/j.ceramint.2011.03.081.
- [53] Zhang, Shan Tao, et al. "Preparation, Structures, and Multiferroic Properties of Single Phase Bi_{1-x}LaxFeO₃ (X=0-0.40) Ceramics." *Journal of Applied Physics*, vol. 100, no. 11, 2006, pp. 3–9, doi:10.1063/1.2390625.
- [54] Goodenough, John B. *Magnetism and chemical bond*. Vol. 1. Interscience Publ., 1963.
- [55] Hill, Nicola A., Pio Bättig, and Claude Daul. "First principles search for multiferroism in BiCrO₃." *The Journal of Physical Chemistry B* 106.13 (2002): 3383-3388.
- [56] Huang, Ji Zhou, et al. "Effect of Mn Doping on Electric and Magnetic Properties of BiFeO₃ Thin Films by Chemical Solution Deposition." *Journal of Applied Physics*, vol. 106, no. 6, 2009, doi:10.1063/1.3225559.
- [57] *BET Surface Area – Andy Connelly*. andyjconnelly.wordpress.com/2017/03/13/bet-surface-area/.